Translational changes upon aging and dietary restriction in progeroid DNA-repair-deficient mice

Authors

Ivar van Galen[1,2], Rutger A. Ozinga[1,2], Damon A. Hofman[1,2], Jip van Dinter[1,2], Sem A.G. Engels[1], Kimberly Smit[1,2], Sebastiaan van Heesch[1,2], Jan H.J. Hoeijmakers[1,2,3,4], Wilbert P. Vermeij[1,2,#]

Affiliations

[1]Princess Máxima Center for Pediatric Oncology, Utrecht, Netherlands

[2]Oncode Institute, Utrecht, Netherlands

[3]Department of Molecular Genetics, Erasmus MC Cancer Institute, Erasmus University Medical Center Rotterdam, Rotterdam, Netherlands

[4] Institute for Genome Stability in Ageing and Disease, Cologne Excellence Cluster for Cellular Stress Responses in Aging-Associated Diseases (CECAD), University of Cologne, Cologne, Germany

[#] Correspondence to Wilbert P. Vermeij; W.P.Vermeij@prinsesmaximacentrum.nl

Keywords: dietary restriction, translation dynamics, DNA damage and repair, ribosome profiling, aging, mice

Abstract

Aging is a complex multifactorial phenomenon largely driven by damaged macromolecules. We showed recently that with aging time- and exposure-dependent accumulation of DNA damage derails the basal process of transcription physically stalling RNA polymerase, lowering and skewing the transcriptional landscape in a gene-length-dependent fashion. However, how this influences the translational output and whether translation is similarly affected is largely unknown. Here, we present a parallel analysis of transcriptional and translational liver profiles from the well-characterized *Ercc1*$^{\Delta/-}$ progeroid, DNA repair-deficient mouse model compared to wildtype under ad libitum conditions and upon dietary restriction (DR), which strongly delays aging in this mutant.

Using ribosome profiling, we found that transcriptional changes during accelerated, normal, and delayed aging are largely preserved at the translational level ruling out a major translational impact on gene expression in aging. Moreover, in both *Ercc1*$^{\Delta/-}$ and aged wild-type mice there was a prioritization of inflammation, metabolic redesign, and expression of translation initiation factors, along with a shift in codon occupancy. While translation initiation factors were further increased by DR, absolute codon occupancy was partially normalized showing a discordant response. Additionally, increased ribosomal pausing and a relative reduction of upstream open reading frame expression were both further intensified by DR.

Together these data infer a finetuning of the translational output, e.g. by regulating upstream open reading frames under various cellular stress situations. This study uncovers a complex interplay between DR, DNA damage, aging, and translational regulation, highlighting the potential of DR to modify DNA damage-driven translational dynamics during aging.

Introduction

Genomic instability has been posited as central hallmark of aging and is characterized by the accumulation of a wide range of DNA lesions[1,2]. While most DNA lesions are efficiently resolved by their respective repair systems, some damages escape recognition, are irreparable or repaired incorrectly, leading to the accumulation of mutations and persistent DNA lesions with age[1,3]. This DNA damage drives systemic aging by physically blocking transcription, leading to a lower and particularly imbalanced gene length dependent transcriptional output[3–5], and since transcription is essential for every cellular process, this age-related phenomenon of genome-wide transcription stress indirectly affects major aging hallmarks[4,6,7].

Next to a disbalanced transcriptional output does aging induce a general decoupling between the transcriptome and proteome[8–11]. Furthermore, aging is associated with a dysregulation of proteostasis and a reduction in protein biosynthesis across diverse tissues and organisms[12,13], and can be further altered during age-related diseases[14,15]. Age-driven changes also extend to the stoichiometry of protein complexes, such as the cytosolic ribosome complex, where both a dysregulation between transcript and protein levels, as well as a stoichiometric loss between subunits has been reported[10]. Additionally, aging influences translational dynamics, leading to increased ribosome pausing and collisions, shifts in transcript coverage at start and stop codons, and alterations in the translation of upstream open reading frames (uORFs)[16–19], culminating in a reduced and altered translational profile[20]. Interestingly, DNA damage has been implicated in many of the above processes including derailed transcription[4], inhibited translation[21], and ribosome stalling[22], subsequently contributing to inflammation[23]. However, how DNA damage impacts translation, in relation to the before mentioned age-related gene length dependent transcriptional imbalance, is largely unknown.

To assess the effect of aging and accumulating DNA damage at the level of translation, we compared side-by-side mRNA- and Ribo-seq. For this, we used the well-characterized *Ercc1*$^{\Delta/-}$ DNA-repair-deficient progeroid mouse model[5,24–26]. These mice harbor a single allele coding for a truncated yet partially active ERCC1 variant, a crucial factor involved in multiple DNA repair pathways. The dysfunctional ERCC1 in these mutants leads to a broad variety of unrepaired persisting genomic lesions, accelerating the aging process systemically and limiting their lifespan to 4-6 months[27]. Remarkably, a 30% dietary restriction (DR) regimen, the only evolutionary conserved intervention for extending health and lifespan across multiple species, has been shown to partially mitigate transcriptional aberrations in *Ercc1*$^{\Delta/-}$ mice, prolonging their lifespan up to 200% and strongly delaying the onset of numerous age-related phenotypes[5].

To elucidate if and how transcriptional changes in progeroid *Ercc1*$^{\Delta/-}$ mice are altered at the translational level, we utilized ribosome profiling, a technique that captures a snapshot of active translation. Additionally, we investigated how DR, which partially alleviates DNA damage and consequently decelerates aging in these animals, modulates these dynamics, thereby providing

insights into the interplay between diet, DNA damage, and translation in the context of DNA damage-driven aging.

Results

Transcription and Translation are Influenced by Genotype and Diet

To investigate active translation during DNA-damage-driven accelerated aging and the anti-aging effects of dietary restriction (DR), we selected liver as primary organ of interest due to its key role in metabolism, detoxification and the extensively characterized transcriptional landscape during aging in both wild-type (WT) and *Ercc1*$^{\Delta/-}$ progeroid DNA-repair-deficient mice[4,5,28,29]. To capture the progeroid aging phenotype effectively, we focused our analysis on 16-week-old male mice, an age at which *Ercc1*$^{\Delta/-}$ mice exhibit pronounced aging characteristics but prior to becoming overtly moribund[27] and the benefits of DR and weight changes are very prominent[5]. The experimental setup encompassed: *ad libitum* (AL) feeding and 30% DR, maintained over the last ~8 weeks (Fig. 1A, S1), which we previously showed to strongly improve health and transcriptional aberrations[5].

Our ribosome profiling data showed a clear 28nt footprint preference with about half of all reads considered “clean” as they did not map to tRNA or rRNA sequences (Fig. 1B-C). After in-silico removal of tRNA- and rRNA-contaminants, QC revealed >80% of reads mapped to coding sequences (Fig. S1B) while showing a strong P-site-specific frame preference indicative of normal tri-nucleotide footprint periodicity (Fig. 1D-E). A high-quality mRNA sequencing dataset was generated from the same liver samples, to facilitate direct comparison between mRNA- and ribo-seq data (Fig. S1C).

Principal Component Analysis (PCA) of both mRNA and ribo-seq data showed distinct clustering and uniformity within and between groups, with primary differentiation based on genotype and diet (Fig. 1F-G, S1D-E). Ribo-seq data demonstrated overall somewhat smaller variations among samples from the same group, showing greater homogeneity within and separation between each group compared to the mRNA-seq data. Notably, group distributions for both datasets showed a highly similar arrangement, and the proportional variance of PC1 and PC2 was comparable in both datasets. Thus, these results indicate overall data quality was of high quality and that PCA analysis effectively differentiated the experimental groups, underscoring the distinct characteristics within the data with a highly similar transcriptional and translational output.

ERCC1-Deficiency Modifies Metabolic and Inflammatory Pathways

When directionality and fold-change differences between *Ercc1*$^{\Delta/-}$_AL and WT_AL at the transcriptional level were compared with those at the translational level, a high degree of concordance was observed (Fig. 2A), indicating that globally, translation largely mirrored the

transcriptional profile and that translational regulation was limited. Further analysis of the effect of ERCC1-deficiency identified a similar number of significantly differentially transcribed (n=2429) and translated (n=2288) genes, with a 45.0% overlap between the two datasets. At both the transcription and translational level, Ingenuity Pathway Analysis (IPA) revealed in the class of upstream regulators a decrease in PPARA and increases in STAT5B, TNF, TP53 and IFNG (Fig. 2B-C), indicative of elevated inflammation/toxicity. Interestingly, when comparing mRNA- and Ribo-seq, the class of immune-related regulators appears more prominent in translation. Immunoglobin, IFN, Interferon alpha have all strongly moved up in the ranking and TGF1, which shows a down-trend in transcription, is upward in translation, consistent with the idea of prioritization of immune responses and a capacity for fine-tuning at the level of translation. Metabolic processes were generally downregulated, except for cholesterol biosynthesis and pathways related to its precursors[30], like mevalonate and zymosterol, which in turn were upregulated (Fig. S2A-B). These findings were mirrored by the specific upregulation of 'LPS/IL-1 mediated inhibition of RXR function', which is associated with impaired lipid metabolism and transport[31,32]. The connection of these pathways to the acute phase response, a response triggered by infection, tissue injury, or inflammation[33,34], was apparent in our context of constitutive DNA damage and further supported by increased p53 signaling (Fig. 2D-E). For these processes the ranking in transcription was largely preserved in translation. Importantly, similar concordantly affected pathways and processes were observed when comparing natural aged 104-week-old WT animals to young 16-week-old controls (Fig. S1A, S2C-I).

ERCC1-Deficiency Alters Translational Dynamics and Open Reading Frame Translation

Natural aging affects various aspects of translation, including fidelity and kinetics[18]. Evaluating the expression of essential components of the translation machinery in *Ercc1*$^{\Delta/-}$_AL mice revealed a significant increase in translation initiation factors (Fig. 3A, supplemental file 1), while cytoplasmic and mitochondrial ribosomal subunits were not differentially translated (Fig. 3B, S3A). A similar pattern was observed in aged WT_AL mice, which in addition did show a significant downregulation of mitochondrial ribosomal subunits (Fig. S3B-D).

Next, we examined ribosome pausing, an important aspect of translation kinetics. This process is characterized by a halt or significant slowdown in ribosomal movement along the mRNA strand during protein synthesis and is quantified by the distance and distribution of ribosomal footprints along the mRNA. Analysis of footprint density yielded ribosomal pause site intensity scores and the number of pause sites per gene transcript. Our data showed a significant increase in pause score intensity (Fig. 3C), but no changes in the number of pause sites per gene (Fig. 3D). Neither of these parameters were significantly altered in old WT_AL mice (Fig. S3F-G).

To gain further insight into translational dynamics, we assessed codon occupancy, a proxy for the frequency and duration of ribosome binding and translation of specific codons within mRNA sequences[35]. Absolute codon occupancy (pre-normalization for amino acid translational abundance and thus indicative of absolute changes in codon usage between groups), revealed

distinct alterations in *Ercc1*$^{\Delta/-}$_AL mice as compared to their wild-type counterparts. Specifically, codons encoding many essential amino acids showed increased occupancy, in addition to nearly all codons for Arginine (R) and Serine (S) (Fig. 3E), but this pattern did not correlate with other amino acid characteristic (Supplemental file 2). Interestingly, a strikingly similar change in absolute codon occupancy was observed in old WT_AL animals, including a notable increase in the ACA codon for threonine (T), which exhibited the highest occupancy in both *Ercc1*$^{\Delta/-}$_AL and aged WT_AL mice (Fig. S3E). In contrast, relative codon occupancy (normalized for differences in amino acid abundance which is indicative of altered codon expression within an amino acids' codon family) largely abrogated the earlier observed changes within *Ercc1*$^{\Delta/-}$_AL and old WT_AL animals when compared to young controls (Fig. 3F, S3F). However, some trends, such as for the codons GCU, GGU, ACU, ACA, remained consistent between relative and absolute codon occupancy.

Next, we examined the translated rates of non-canonical and canonical open reading frames (ORFs) in *Ercc1*$^{\Delta/-}$_AL mice, as these are known to be affected by cellular stressors[36,37]. Upstream ORFs (uORFs), a non-canonical type of reading frame located in the 5' untranslated region (UTR) of mRNAs, have the potential to regulate the translation of downstream canonical coding sequences (CDS). Overlapping uORFs and conventional uORFs tend to inhibit translation of the CDS (Fig. 3G)[36–40]. Relieving this inhibition is part of the cell's adaptive stress response, aiding in homeostatic maintenance and ensuring survival under environmental challenges by enabling enhanced translation of canonical ORFs[41].

In *Ercc1*$^{\Delta/-}$_AL, we identified 101 differentially translated uORF containing transcripts, which were generally downregulated compared to WT_AL (Fig. 3H). Interestingly, a comparative analysis of fold changes between differentially translated uORF and their corresponding canonical CDS revealed that, even though both were downregulated, a markedly stronger translational downregulation happened at the uORF region (Fig. 3I-J, S3K). A similar albeit less intense trend was observed in 104-week-old WT_AL mice (Fig. S3I-J). Additionally, we found a significant overlap between uORFs regulated differentially in accelerated aged *Ercc1*$^{\Delta/-}$_AL and old WT_AL versus young WT controls (Fig. 3K). This overlap showed a set of age-related uORFs whose genes are related to metabolism, cellular stress, and regeneration (supplemental file 3A).

Differences Between *Ercc1*$^{\Delta/-}$ and Old WT Mice

Ercc1$^{\Delta/-}$ mice display an accelerated aging phenotype primarily driven by DNA damage, while natural aging is affected by various stressors including DNA damage. Comparing directionality and fold-change differences of DEGs at the transcriptional and translational level between 16-week-old *Ercc1*$^{\Delta/-}$ and 104-week-old WT mice showed a high degree of concordance (Fig. S4A).

In contrast, IPA upstream regulator analysis showed some disparity between the top mRNA and Ribo results (Fig. S4B-C). While the upstream regulators POR and PPARA were both predicted to be decreased in *Ercc1*$^{\Delta/-}$ and old WT when compared to young WT, which has been reported before for natural aging[42]. Direct comparison of *Ercc1*$^{\Delta/-}$ to old WT showed that POR was

relatively more inhibited in *Ercc1*$^{\Delta/-}$, while PPARA was increase, potentially due to altered lipid metabolism in *Ercc1*$^{\Delta/-}$ mice[43]. *Ercc1*$^{\Delta/-}$ also showed a markedly lower activity of TGFB1 than old WT, which was more pronounced at the transcriptional level. Notably, NFE2L2 and immunoglobulin complex were predicted to be activated in *Ercc1*$^{\Delta/-}$ mice when compared to old WT, in line with the elevated oxidative stress and altered inflammatory signaling reported for this model (Fig. S4B-C)[44].

Analysis of metabolic processes showed that most were relatively increased in *Ercc1*$^{\Delta/-}$ compared to old WT and that they centered around lipid metabolism (as indicated by cholesterol synthesis, fatty acid B-oxidation) and oxidative stress (e.g., increased glutathione-mediated detoxification; Fig. S4D-E). Additionally, signaling pathways were largely lowered and characterized by LPS/IL-1 mediated inhibition, sirtuin signaling, NRF2 oxidative responses (NFE2L2), and NAFLD signaling, all strongly related to stress mechanisms and altered lipid metabolism (Fig. S4F-G)[45,46]. As mentioned above were differences in absolute codon occupancy in *Ercc1*$^{\Delta/-}$ and old WT relatively similar when compared to young WT animals. Direct comparison of *Ercc1*$^{\Delta/-}$ to old WT similarly showed that differences were limited, but that some codon groups (e.g. histidine (H), isoleucine (I), and Tyrosine (Y)) were more highly expressed in *Ercc1*$^{\Delta/-}$ (Fig. S4H). Differences in relative codon occupancy were largely negligible, except for AUA which showed a subtle increase and AUU and UCG which decreased in *Ercc1*$^{\Delta/-}$ (Fig. S4I). Finally, uORF expression was reduced in *Ercc1*$^{\Delta/-}$ mice, with a more pronounced decrease than observed for canonical ORFs (Fig. S4J–K).

DR Partially Reverses Processes Affected in *Ercc1*$^{\Delta/-}$ Mice

DR alleviates genotoxic stress in *Ercc1*$^{\Delta/-}$ mice, likely by triggering a protective, anti-aging "survival" response boosting maintenance and resilience (e.g. anti-oxidant defense)[5,47,48]. To evaluate this scenario, we analyzed the expression and translational parameters affected in *Ercc1*$^{\Delta/-}$_DR mice and assessed DNA damage-related changes relative to AL-fed animals. Comparing DR-regulated changes in ribosome profiling data with mRNA again revealed high similarity and equal variance (Fig. 1F-G, 4A, S5A-F). However, the main advantage of Ribo-seq is its ability to examine various aspects of translation and its dynamics; therefore, we primarily focused on this dataset.

The DR-induced differentially expressed genes (DEGs) in *Ercc1*$^{\Delta/-}$ and WT mice showed significant overlap (Fig. 4B) with more than 95% altered concordantly (Fig. 4C), indicating a highly similar response in both genotypes, consistent with previous findings at the transcript level[5]. However, comparing *Ercc1*$^{\Delta/-}$-induced and DR-driven changes, revealed a different pattern: 64% of overlapping genes were regulated discordantly and thus constituting "rescued" *Ercc1*$^{\Delta/-}$ responses by DR, while the 36% concordant DEGs are likely part of the DR-like "survival" response to cellular stresses (Fig. 4D-E), which we previously found to be induced in *Ercc1*$^{\Delta/-}$ and other repair mutants[47,49].

Upstream regulator analysis of genes differentially translated in *Ercc1*$^{\Delta/-}$_DR vs AL mutants using IPA revealed an inverse response compared to *Ercc1*$^{\Delta/-}$_AL vs WT_AL mice, in line with DR counteracting the accelerated aging effect in *Ercc1* mutants (Fig. 2C, 4F). These regulators included PPARA, POR, and STAT5B which are associated with inflammation and lipid metabolism. While pathway analysis of metabolic processes revealed only subtle changes (Fig. S5G), signaling processes consistently indicated reduced inflammation and improved liver functioning (Fig. 4G). Finally, we found DR to significantly upregulate pathways related to "EIF2 signaling" and the "regulation of eIF4 and p70S6K signaling" in both *Ercc1*$^{\Delta/-}$ and WT genotypes (Fig. 4G-H). Both pathways are characterized by the presence of ribosomal subunits and upregulation of these pathways largely aligned with literature[5,50–52]. Notably, both pathways, essential for the regulation of translation, were not differentially regulated in *Ercc1*$^{\Delta/-}$_AL mice when compared to WT_AL counterparts (Fig. 2D-E).

DR Differentially Regulates Translation Dynamics in *Ercc1*$^{\Delta/-}$ as Compared to WT

We next examined changes to the expression of translation initiation factors and ribosomal subunits in the context of DR in our ribosome profiling data. DR increased the expression of translation initiation factors in both WT and *Ercc1*$^{\Delta/-}$ mice (Fig. 5A, S6A-B). The expression of mitochondrial ribosomal subunits was highly variable within each group but, as mentioned earlier, showed a significant downregulation in WT aging, and DR in *Ercc1*$^{\Delta/-}$ mice significantly reduced subunit levels as compared to DR in WT mice (Fig. S6C-D). In contrast, cytosolic ribosomal subunits were significantly upregulated by DR in both genetic backgrounds and significantly lowered in 7 vs 16-week-old *Ercc1*$^{\Delta/-}$ mice (Fig. 5B, S6E-F).

Investigating the changes in cytosolic ribosomal subunits, we discerned an atypical expression pattern for *Rpl22l1* as the only significantly increased cytosolic ribosomal subunit protein in *Ercc1*$^{\Delta/-}$ mice when compared to WT (Fig. 5C), with an analogous pattern observed in old wild-type animals (Fig. S6G). Additionally, DR revealed a general upregulation of subunits except for two, *Rps27l* and *Rpl36al*, which were specifically downregulated in *Ercc1*$^{\Delta/-}$ by DR but not in WT mice (Fig. 5D, S6H-I). *Rps27l* and its paralog *Rps27* have previously been shown to display an inversely correlated mRNA abundance across various mouse cell types impacting transcript association[53]. Interestingly, only the combination of DR and the *Ercc1*-mutation resulted in the differential expression of these two subunits (Fig. 5E).

Continuing our examination of translational dynamics, we found that the number of pause sites per gene showed a homogenous distribution for all groups with no statistical differences (Fig. 5F, S6J). On the contrary, DR further enhanced the pause score intensity for *Ercc1*$^{\Delta/-}$ but not in WT mice (Fig. 5G, S6K). Finally, DR partially alleviates the absolute non-normalized codon occupancy profile associated with DNA damage and natural aging (Fig. 3E, 5H, S7A). Notably, DR tends to lower the codon occupancy of essential amino acids, and some others such as serine (S) and arginine (R) and the specific ACA codon for threonine (T), potentially reflecting an adaptive

response to resource constraints. This DR profile for absolute codon occupancy was significantly less pronounced in WT mice (Supplemental file 2). Additionally, relative codon occupancy normalized to amino acid abundance revealed that, while overall changes were limited, DR reversed some previously observed trends, including those in GCU, GGU, and threonine codons, between *Ercc1*$^{\Delta/-}$ AL and WT AL mice (Fig. 3F, 5I, S7B). Taken together, the observed changes to the expression of the translational machinery, pause site intensity, and codon occupancy highlight the potential impact of DR on translational dynamics in the context of DNA damage-driven accelerated aging.

DR further downregulates uORF expression in *Ercc1*$^{\Delta/-}$ mice

In addition to the DR-induced changes in translational dynamics, DR drastically increased the number of differentially expressed uORF-containing transcripts in *Ercc1*$^{\Delta/-}$ mice beyond the changes already triggered in AL-fed conditions (Fig. 6A). In general, DR led to the downregulation of many uORF containing transcripts in *Ercc1*$^{\Delta/-}$ mice (Fig. 6B, S7C). In contrast, the effect of DR in WT mice was rather limited (Fig. S7D), although a significant proportion of differentially expressed uORFs noted in DR-fed *Ercc1*$^{\Delta/-}$ and DR-fed WT overlapped (Fig. 6C, Supplemental file 3B). In *Ercc1*$^{\Delta/-}$ mice, but not in WT mice, DR additionally led to the differential inhibition of several uORFs linked to genes related to processes like cellular survival and apoptosis.

As described earlier, was the ratio of uORFs to their canonical ORF expression reduced in *Ercc1*$^{\Delta/-}$ mice. DR further reduced this ratio in *Ercc1*$^{\Delta/-}$ mice, but only marginally in WT mice (Fig. 6D, S7E-G). Quantification of these ratios showed a clear pattern where stress situations reduced the ratio of uORF to canonical ORF expression (Fig. 6E, S7H). This suggests that the interaction between uORF expression and canonical ORF translation is amplified in the context of stress resilience and is particularly evident under conditions of multiple concurrent stressors.

Discussion

Aging induces a variety of changes, including genome-wide transcriptional decline, preferentially affecting long genes, demonstrated first in progeroid DNA repair-deficient *Ercc1*$^{\Delta/-}$ mice and later also with natural aging in numerous species, strengthening the relevance of accelerated aging for understanding normal aging[4–7,54,55]. Using liver as well-characterized organ central to metabolism, we investigated here whether and to which extent these transcriptional changes are counteracted at the translational level or whether translation degenerates as well. Our findings indicate that transcriptional output is largely retained at the translational level in both *Ercc1*$^{\Delta/-}$ and WT mice, regardless of diet or age. In the liver of *Ercc1*$^{\Delta/-}$ mice we observed significant alterations in processes linked to inflammation and metabolism. Many of these responses are stress related [56,57], and likely triggered by sterile inflammation in response to DNA damage[7,58–60]. Some consequentially altered metabolic pathways could be detrimental. For example, increased AhR

signaling activity has been inversely linked to NAD+ metabolism[61,62], while NAD+ supplements have been shown to extend health and lifespan of mice, including DNA-repair-deficient models[63–67]. Interestingly, many alterations were influenced in an age-related, DNA-damage-dose-dependent manner, while 30% DR ameliorated a variety of tissue-damage-related pathways in *Ercc1*$^{\Delta/-}$ mice, findings that are logically consistent with the anti-aging benefits exerted by DR[5]. Notably, DR influenced translational regulators 'eIF2 signaling' and 'regulation of eIF4 and p70S6K signaling'[50,68,69], which were predominantly enriched for ribosomal subunits. The increased phosphorylation of eukaryotic translation initiation factor eIF4 has recently been linked with translation of mRNAs involved in fasting-induced lipid catabolism and ketone body production, via a newly-discovered lipid-induced AMPK–MNK–eIF4E kinase signaling pathway[50], which aligns with the observed differential regulators and pathway expression in our study.

The distinct expression of certain cytosolic ribosomal subunits under conditions of DNA damage and DR draws attention to potentially unique functions related to translation. Increased expression of *Rpl22l1* during WT and accelerated aging is noteworthy, as it has previously been implicated in processes like proliferation, translation, and epithelial-to-mesenchymal transition[70–72], likely linked to damage-induced cellular turnover. Moreover, DR modified *Rps27l* expression which has previously been associated with p53 signaling and autophagy[53,73,74]. Concurrently, *Rpl36al* has been postulated to play a role in peptide bond formation and is the only ribosomal protein so far identified that can engage with tRNA, regardless of its ribosomal association[75]. Notably, DR specifically influenced the expression of Rps27l and Rpl36al during conditions of DNA-damage-driven cellular stress but not in young WT, suggesting a synergistic requirement of DNA damage accumulation and nutrient stress.

Curiously, the translation of ribosomal subunits in the liver of naturally aged C57BL/6 mice (32 months) has previously been reported to decrease through inhibition of 5'-TOP related genes [16]. In contrast, our results demonstrate that DR can increase both the transcription and translation of the translational machinery, while other studies in different animals have reported similar increases at the transcriptional level[10,76].The reason for this discrepancy is yet unknown but might be related to the improved health in mice with a more outbred like C57BL6J/FVB hybrid background as compared to the pure C57BL6J strain. Future work might compare relevant datasets to exclude other aspects such as differences in data handling, normalization, or validate findings more at an absolute quantitative level.

The general upregulation of initiation and cytosolic ribosomal subunits could reflect an attempt to increase ribosomal turnover, enhancing translational regulatory oversight and fidelity, or might be an apparent increase due to the relative nature of sequencing when total transcription and translation decreases. Additionally, the absence of changes in mitochondrial ribosomal subunits presents a striking dichotomy, suggesting a disconnect between the regulatory adjustments of cytoplasmic and mitochondrial ribosomal subunits under DR, warranting further

examination, also considering the reduced correlation in age-related changes in transcriptome versus proteome[10].

Furthermore, translation dynamics were also influenced, with pause site intensity, absolute codon occupancy, and uORF expression being more strongly affected by ERCC1-deficiency than by WT aging, consistent with known phenotypical differences[27,63]. Moreover, DR in young WT mice showed little effect on various aspects of translational dynamics, while having a strong impact on *Ercc1*$^{\Delta/-}$ mice, further supporting the idea of synergistic interactions in responses between genotoxic- and nutrient-induced cellular stress. Codon occupancy showed a clear discrepancy between the effects caused by the *Ercc1*$^{\Delta/-}$ mutation and DR, with DR reversing the pattern towards AL-fed WT levels. Although correlations with essential amino acid and codon usage were observed, direct mechanistic explanations remain unidentified.

Both relative codon occupancy and ribosomal pausing are linked to ribosomal movement, yet they displayed discordant behavior. However, pause score intensity and relative uORF changes were both concordantly intensified by DR in *Ercc1*$^{\Delta/-}$ mice, suggesting that these processes are potentially beneficial adaptive mechanisms to ensure efficient protein synthesis despite DNA damage and nutrient scarcity. Ribosomal pausing is for example an important aspect of translation, affecting protein folding, localization, fidelity, and protein expression by altering the speed of translation elongation[19,77]. However, exacerbation of pausing, i.e. ribosomal stalling, during aging has been suggested to disrupt co-translational proteostasis and induce detrimental age-related translational reprogramming potentially leading to reduced levels of vital proteins and an exacerbation of the aging phenotype in neurological tissues, complicating its mechanistic role[17,22,79]. It remains to be investigated if DNA damage could be an antagonistic pleiotropic regulator, where mild levels of genotoxic stress reduce the speed of translation, while excessive damage drives proteotoxic stress, and whether these effects could be tissue dependent[3,24,78].

A large number of canonical ORFs associated with the uORFs we observed are known to produce proteins crucial for cellular homeostasis. The relative reduction of these uORFs, compared to their canonical counterparts, suggests a protective or adaptive mechanism. Interestingly, uORF-related gene transcripts can also contain other regulatory elements like internal ribosome entry sites (IRES), which are often found in mRNAs coding for master regulators of cellular homeostatic responses. These mRNAs must be tightly controlled, and under various stresses, including DNA damage and amino acid starvation, the relative increased selective translation of these sequences ensures homeostasis[80]. Moreover, while the observed uORF changes are statistically significant, the relatively low number of uORF-related footprints and their potential interaction with IRES elements suggests that further research, potentially involving deeper sequencing, may provide additional insights.

Models of accelerated aging often do not fully encapsulate all aspects of natural physiological aging[3,24,78,81]. However, the *Ercc1*$^{\Delta/-}$ mouse model shows strong similarities with natural aging at both the molecular and physiological level[25,82,83], and similarly displays accelerated

glycan- and epigenetic ageing clocks across multiple tissues[84–86]. In the current study, differences between accelerated and naturally aged mice were mainly characterized by lipid metabolism. Given the central role of lipid metabolism in longevity, these differences may be partially explained by survival-bias-driven metabolic adaptations in the naturally aged mice, distinguishing them from the broader cohort.

In previous work, we have shown that aging in both *Ercc1*$^{\Delta/-}$ and wild-type mice is correlated with a gene length dependent transcriptional decline due to physical stalling of elongating RNA-polymerases leading to a disbalance between long and short genes[4]. In the present study, we found a high similarity between transcriptional and translational profiles, suggesting that most of the gene length dependent transcriptional changes are likely 'translated' to the protein level. Another feature, which is widely associated with aging but has remained largely elusive, is a progressive decoupling between the transcriptome and proteome[10,87,88]. At first sight this might seem difficult to rationalize with our observations, however, continuation of a gene length dependent disbalance onto the protein level might lead to incomplete multi-subunit protein complexes, when one subunit derived from a larger gene is under expressed due to transcription mentioned above. Incomplete protein complexes can in turn trigger the unfolded protein response and induce degradation of the affected subunits[89,90] or trigger compensatory mechanisms[91]. Since cells contain numerous protein complexes, this might partially explain the disconnect between the transcriptome and proteome during aging. Future studies should investigate whether gene length–dependent transcriptional decline contributes to the loss of proteostasis during aging, to evaluate the validity of this hypothesis. Moreover, the role of RNA damage driven ribosome collision herein and its contribution to aging and related changes remains to be further investigated[92–94].

In conclusion, our data showed that DR in *Ercc1*$^{\Delta/-}$ mice elicited a multifaceted adaptive response, revealing alterations across several molecular pathways, including inflammation, protein synthesis, and cellular metabolism, while demonstrating the adaptive capacity of the translational machinery under conditions of stress and nutrient limitations. Moving forward, the influence of dietary composition, RNA homeostasis, and the proteome, should be examined to shed further light on the interplay between genomic instability, metabolism, translational control, and lifespan.

Methods

Mouse models and ethics statement

Male *Ercc1*$^{\Delta/-}$ and wild-type (WT) littermate control *(Ercc1*$^{+/+}$*)* mice were obtained by crossing *Ercc1*$^{\Delta/+}$ (in a pure C57BL6J or FVB background) with *Ercc1*$^{+/-}$ mice (in a pure FVB or C57BL6J background respectively) to yield *Ercc1*$^{\Delta/-}$ offspring with a genetically uniform F1 C57BL6J/FVB hybrid background. These two backgrounds were crossed to minimize unfavorable characteristics, like early onset of blindness in an FVB background or deafness in a C57BL6J background. Since *Ercc1*$^{\Delta/-}$ mice were smaller, food was administered within the cages and water bottles with long nozzles were used from around two weeks of age. Experiments were performed in accordance with the Principles of Laboratory Animal Care and with the guidelines approved by the Dutch Ethical Committee in full accordance with European legislation (DEC no. 139-12-13 and 139-12-18).

Housing conditions and dietary regimens

Animals were housed individually in ventilated cages under specific pathogen-free conditions, in carefully controlled environments (20–22 °C, 12h light:12h dark cycle). Mice were visually inspected daily and weekly weighed and scored blindly for gross morphological and motor abnormalities. All animals were bred and maintained on AIN93G synthetic pellets (Research Diet Services B.V., Wijk bij Duurstede, The Netherlands; gross energy content 4.9 kcal/g dry mass, digestible energy 3.97 kcal/g). On average, 6-16 week old *Ercc1*$^{\Delta/-}$ mice ate 2.3 g food per day. The animals that were given dietary restriction (DR) were so from 7 weeks of age, when development was largely completed, starting with 10% restriction. DR was gradually increased weekly with 10%, until 30% DR (1.6 g/day), which was provided from 9 weeks of age onward as previously published[5]. Adult WT mice ate on average 3.0 g food per day, resulting in 2.1 g/day for 30% DR and a reduction in bodyweight (Fig. S1F). To avoid alterations in the biological clock, food was provided to the animals just before the start of the dark (active) period, Zeitgeber Time (ZT) 12:00, except for the day of sacrifice, when no food was given prior to collect.

At 16 weeks of age, WT and *Ercc1*$^{\Delta/-}$ mice on AL and DR regimens were sacrificed at the beginning of the dark period between ZT13 and ZT16. Additionally, a group of AL-fed 7-week-old *Ercc1*$^{\Delta/-}$ mice was included, representing a biologically younger age and as control for the start of DR, and a group of AL-fed 104-week-old WT, for comparison to natural aging (Fig. S1A). Prior to weaning, animals were randomly divided over all groups to prevent selection bias. Animals were euthanized when necropsy age was reached, livers were snap frozen in liquid nitrogen, and stored at −80°C for molecular analysis.

mRNA sequencing

Snap-frozen liver specimens were lysed in QIAzol lysis reagent with the TissueLyser LT (QIAGEN) and RNA was isolated using the miRNeasy mini kit (QIAGEN; 217004) according to manufacturer's protocol with optional on column DNase I treatment (QIAGEN; 79254). RNA quality and quantity were assessed using the NanoDrop One (Thermo Fisher Scientific, USA) and Bioanalyzer 2100 (Agilent, Santa Clara, CA, USA; G2939BA), respectively. RNA integrity values ranged between 8.4 and 9.5. Samples were sent for mRNA paired end 2*150bp sequencing (Novogene, Cambridge, United Kingdom) on the Illumina NovaSeq6000 platform to a depth varying between 39887891 and 63618955 total reads per sample.

Ribosome profiling

Snap frozen tissue samples from the same livers as used for mRNA sequencing were used to perform ribosome profiling with minimal modifications as previously described[95,96]. Samples were powdered with a BioSpec Pulverizer (#59012MS) on dry ice. Pulverized material was lysed with 500ul ice-cold lysis buffer (20 mM Tris-Cl pH 7.4, 150 mM NaCl, 5 mM MgCl2, 1% Triton X-100, 0.1% IGEPAL CA-630 (Sigma-Aldrich, USA), 1 mM DTT, 10 U/ml RNase-free DNase 1 (Lucigen, USA), 100 µg/ml cycloheximide (Sigma-Aldrich, USA)) for 15 minutes on ice, triturated ten times through a 23G needle, and clarified through centrifugation at 20000 g at 4 °C for 10 min. Total RNA content of sample lysates was estimated using the Qubit™ RNA broad range (BR) Assay Kit (Thermo Fisher Scientific, USA) on an Invitrogen™ Qubit™ 4 fluorometer (Thermo Fisher Scientific, USA). Lysates were then digested per 200 µl aliquots with RNAse I (10 units per 20 µg of RNA; Lucigen, USA) for generation of ribosome-protected fragments (RPFs) at 20 °C for 45 min while shaking at 400 RPM on a thermomixer. The digestion reaction was stopped by adding 5 µl (5U) of SUPERase*In RNAse inhibitor (Thermo Fisher Scientific, USA) and placing the samples on ice. Digested lysates were transferred to Microspin S-400 HR sephacryl columns (Sigma-Aldrich, USA) equilibrated with 3 ml of cold RNase-free polysome buffer (20 mM Tris-Cl pH 7.4, 150 mM NaCl, 5 mM MgCl2) and centrifuged at 600g at room temperature for 2 min. 10 µl 10% SDS was added to the digested lysates and RPFs were extracted using 3 volumes (660 µl) of Trizol LS (Fisher Scientific, USA), followed by addition of 1 volume (880 µl) of ethanol and RNA purification using the Zymo Direct-zol RNA micro prep kit (Zymo Research, USA) with slight modifications to the manufacturer's instructions: Columns were spun dry for 1 min at 12000 g and isolated RPFs were eluted in 20 µl nuclease-free water (Sigma-Aldrich, USA).

Depletion of rRNA was performed using RiboPOOL technology (siTOOLs Biotech; riboPOOL ribo-seq cat# dp-K012-000052, Germany) with a slight modification to the manufacturer's instructions: 200 pmol of RiboPOOL and 100 µl of beads were used per sample. Next, RNA was purified using the Zymo RNA Clean and Concentrator-5 kit (Zymo Research, USA) and size-selected through denaturing PAGE using 15% TBE-Urea gels (Thermo Fisher Scientific, USA). RNA fragments corresponding to 26–34 nucleotides were excised and recovered from gel slices by crushing the gel and rocking at 20 °C, 700 RPM for 2 hours on a thermomixer. RNA

solutions were transferred to Costar Spin-X filter tubes (Thermo Fisher Scientific, USA) and filtered through centrifugation at 2350 g for 6 min. 2 µl of GlycoBlue (Thermo Fisher Scientific, USA) and 700 µl of isopropanol were added per aliquot and RNA was left to precipitate overnight at −80 °C.

Following precipitation, RNA fragments were pelleted by centrifugation at 21130 g at 4 °C for 45 min. Pellets were washed with 1ml of 80% ice-cold ethanol and centrifuged at 21130 g at 4 °C for 10 min. RNA pellets were air-dried for 3-4 min and dissolved in 60.75 µl nuclease-free water on ice. RNA fragments were dephosphorylated using 30 U of T4 PNK (Lucigen, USA) for 1 h at 37 °C and purified using Zymo RNA Clean and Concentrator-5 kit (Zymo Research, USA), where isolated RNA fragments were eluted in 9.5 µl nuclease-free water. Purified fragments were ligated to a pre-adenylated 3'oligonucleotide linker using 100 U of T4 RNA ligase 2 Deletion Mutant (Lucigen, USA) and 5 U T4 RNA ligase 1 (Thermo Fisher Scientific, USA) at 23 °C for 3 h. Leftover linker was removed using 5'Deadenylase (New England Biolabs, USA) and Rec J Exonuclease (Lucigen, USA). Linker-ligated RNA fragments were reverse-transcribed into cDNA using EpiScript reverse transcriptase (Lucigen, USA). cDNA was treated with Exonuclease I (Lucigen, USA) for 30 min at 37 °C, followed by 15 min at 80 °C with a reduction to 4 °C; and further treated with 5 U of RNAse I (Lucigen, USA) and 2.5 U of Hybridase Thermostable RNase H (Lucigen, USA) at 55 °C for 5 min followed by an incubation step at 4 °C to stop the reaction. Treated cDNA was purified using the Zymo Oligo Clean and Concentrator Kit (Zymo Research, USA) with modifications to the manufacturer's instructions: Columns were spun dry for 1 min at 21130 g and isolated RPFs were eluted in 9.5 µl nuclease-free water (Sigma-Aldrich, USA).

Size-selection of cDNA containing ligated linkers was performed through denaturing PAGE using 10% TBE-Urea gels (Thermo Fisher Scientific, USA). cDNA fragments corresponding to 70–80 nucleotides were excised and extracted with ammonium acetate and SDS, followed by overnight precipitation with isopropanol as described above. Size-selected cDNA was circularized for 3 h at 60 °C using 100 U of circLigase I (Lucigen, USA) followed by heat inactivation for 10 min at 80 °C and amplified using Phusion high-fidelity polymerase (New England Biolabs, USA) with reverse primers containing unique barcode sequences for 10 cycles of: 30 sec at 98 °C, 15 sec at 94 °C, 5 sec at 55 °C, 10 sec at 65 °C. Following amplification, 5 µl of 3 M NaCl (Thermo Fisher Scientific, USA), 1 ml of ethanol and 2 µl of GlycoBlue (Thermo Fisher Scientific, USA) were added to each aliquot of cDNA and left to precipitate overnight at −80 °C as described above.

Amplified cDNA libraries were size-selected using 8% non-denaturing TBE-Urea gels (Thermo Fisher Scientific, USA). cDNA libraries corresponding to 150 nucleotides were excised and recovered from gel slices by crushing and subsequent rocking at 37 °C at 700 RPM on a thermomixer for 2 hours. cDNA solutions were transferred to Costar Spin-X filter tubes (Thermo Fisher Scientific, USA) and filtered through centrifugation at 2350g for 6 min. cDNA libraries were purified using the Zymo DNA Clean and Concentrator-5 kit (Zymo Research, USA) with modifications to the manufacturer's instructions: Columns were spun dry for 2 min at 12000 g and isolated RPFs were eluted in 13 µl nuclease-free water (Sigma-Aldrich, USA).

cDNA libraries were quantified using Qubit™ DNA high sensitivity (HS) Assay Kit (Thermo Fisher Scientific, USA) according to the manufacturer's instructions on an Invitrogen™ Qubit™ 4 fluorometer (Thermo Fisher Scientific, USA) and Bioanalyzer 2100 (Agilent) using the High Sensitivity DNA kit and pooled in equimolar ratios. Sequencing was performed on a NextSeq2000 (Illumina; 1x50bp) at the Utrecht Sequencing Facility (USEQ) to a depth varying between 37831148 and 70879824 total reads per sample.

mRNA- and Ribo-seq data processing

Quality control of Ribo-seq data was performed by filtering reads for mitochondrial, rRNA and tRNA sequence contaminations using Bowtie2 v2.4.2 (default settings, except; –seedlen 25)[97]. The resulting ribosome-protected fragments were consecutively aligned to the genome with STAR (version 2.7.3, default settings, except; sjdbOverhang 29, --outFilterMismatchNmax 2, --outSAMattributes = All, --outSAMtype SortedByCoordinate, --limitOutSJcollapsed 10000000, --limitIObufferSize 300000000, --alignSJoverhangMin 1000). RiboseQC v1.1[98] (default settings, except; read_subset = False, fast_mode = False) was used to check the quality of Ribo-seq samples and to extract footprint length distributions, periodicity (3nt codon movement), and P-site counts from uniquely mapped reads. Quality control of mRNA data was performed with with FastQC v0.11.9.

For subsequent expression analysis mRNA reads were treated as single-end and truncated to 28nt to imitate ribosome-protected fragments. Next, both mRNA and ribo-seq datasets were treated identically and processing of raw sequencing reads was performed on our in house-generated data analysis pipeline. Removal of sequence adaptors, tRNA, and rRNA from both mRNA- and Ribo-seq and truncation of mRNA reads was performed using Trimmomatic (version 0.39). Trimmed reads were aligned to the coding region (CDS) of the mouse reference genome (annotation: gencode.vM20.annotation.gtf; genome: GRCm38.p6.genome.fa; http://gencodegenes.org/mouse/release_M20.html) using STAR (version 2.7.3). Read counts for each gene were obtained using FeatureCounts (as part of SubRead version 1.6.4), filtered using filterByExpr with count set to 10, followed by TMM normalization, quantification of log fold changes (logFC), and false discovery rates (FDR) using EdgeR (version 3.32.1). Statistically significant changes in mRNA- and ribo-seq data are referred to as differentially expressed genes (DEGs), depending on context.

For ORF quantification, ribosome-profiling adapters were clipped from reads and filtered for the standard quality threshold used by CutAdapt v3.4[99]. Fragments shorter than 25 nucleotides were discarded and reads were filtered for contaminants using bowtie v2.4.2 as described above. The RPFs were mapped to the mouse genome (annotation: gencode.vM20.annotation.gtf; genome: GRCm38.p6.genome.fa; http://gencodegenes.org/mouse/release_M20.html) using STAR v2.7.8a and analyzed with ORFquant using default settings[100]. All CDS regions from the ORFquant output were analyzed for potential P-sites across all three frames by a custom Python

script. In-frame P-sites were retained, yielding one nucleotide (NT) position per codon. An intersection operation was performed on the resulting BED file with the actual P-sites per sample calculated by ORFquant, providing the number of P-sites present per transcript per sample. Finally, logFC and FDR were calculated with EdgeR (version 3.32.1). Example images of canonical ORF and uORF translation were generated using the Integrative Genomics Viewer (IGV) by normalizing coverage data calculated by ORFquant[101].

Data analysis

Principal Component Analysis (PCA) was employed on the data normalized and mapped to coding sequences (CDS). We used the R - Bioconductor packages 'prcomp' and 'gplots' for PCA analysis and plot generation respectively. Enrichment analysis of pathways and upstream regulators was conducted using overrepresentation analysis (ORA). This process was facilitated through the Interactive Pathway Analysis (IPA) software (Ingenuity Systems, QIAGEN), designed to manage complex genomics data. For these analyses, we utilized a pre-filtered list of differentially expressed genes, selecting those with an FDR≤0.05 and log(FC) > |0.5| to denote differential expression. Upstream regulator results were filtered to only include genes, RNAs, and proteins while excluding, e.g., drug compounds, with Z-scores indicating the likely activation state of biological function. The identification of over-represented canonical pathways was achieved based on the data in the Ingenuity Pathways Knowledge Base. In IPA, gray bars represent pathways where activity predictions are not possible, while white bars indicate pathways with z-scores near zero or those ineligible for analysis due to fewer than four analysis-ready molecules (z-score = NaN).

GSEA (v4.3.2 – build 13, standalone version) was run using TMM-normalized CPM values as input. For each comparison between groups (as shown in the figures), genes were ranked by signal-to-noise ratio, and enrichment scores were then calculated for predefined gene sets comprising annotated mitochondrial and cytosolic ribosomal subunits and translation initiation factors (Supplemental File 1)[102]. Collapse/Remap to gene symbols was set to 'No_collapse' and permutation type was set to 'gene_set' to improve workflow for NGS data. All other settings were left at default.

Differential translational efficiency was examined using the DeltaTE software tool with standard settings and 'batch' set to 0[103]. Genes were deemed differentially translated if they exhibited an FDR≤0.05. Pause site prediction and P-site codon occupancy were analyzed by the respective modules from Ribotoolkit using default settings[35]. Pause site prediction was powered by PausePred, which calculates the number of reads mapped to each position within a sliding window of length 1000 (step = length / 2), considering footprints of 28-30nt, normalizes these values over the average read density within the window, and computes the pause score as the average across overlapping windows[104]. For quantification of pause scores, those genes were used for which a pause score could be calculated in all genes using a default pause score threshold of 20 (n=1228 genes). P-site codon occupancy was calculated with ribotoolkits and referenced to

as “absolute codon occupancy” as values are not automatically normalized for amino acid abundance. After normalization for differences in amino acid usage outside of ribotoolkits, the data was referenced to as “relative codon occupancy”. Heatmaps were based on edgeR normalized data and z-score transformed for visualization. Heatmaps based on ratio comparisons were LOG2 transformed before z-score transformation.

Statistics

Statistical analyses were performed using GraphPad Prism (GraphPad Software, La Jolla, CA, USA; version 9.2.0), DeltaTE[103], Ribotoolkit[35], IPA (Ingenuity Systems, QIAGEN), GSEA (v4.2.3 Build 10), or R Studio (2021.09.1, build 371). Significant p values were expressed as *p≤0.05, **p≤0.01, ***p≤0.001, ****P≤0.0001. All data with error bars are presented as mean ± standard deviation (SD) as specified in figure legends. Nonparametric statistical analysis was applied to pause score analysis as the data was not normally distributed. Statistical differences in pause score violin plots with two groups were calculated using Mann-Whitney unpaired test in GraphPad Prism. Statistical differences in pause score violin plots comparing >2 groups were calculated using one-way ANOVA and multiple comparisons testing was corrected for using Dunn’s test also in GraphPad Prism. Statistical significance and enrichment levels for the overlapping sections of the Venn diagrams were calculated using a custom R script based on hypergeometric distribution, as previously described[105]. Pie chart statistics were calculated based on cumulative binomial distribution probabilities.

Author contributions

IvG, JHJH, WPV conceptualized and designed the study IvG, SAGE, KS performed wet lab experiments. IvG, RAO, DAF, JvD performed dry lab experiments and statistical analysis of data. IvG, SvH, JHJH, WPV wrote the manuscript, and RAO, DAF, JvD, SAGE, KS contributed to editing the manuscript. All authors contributed to the article and approved the submitted version.

Acknowledgments

We are grateful to Renata Brandt, Sander Barnhoorn and the animal caretakers for general assistance with mouse experiments and Irene van Dijken and Willianne Vonk for experimental support. This research was funded by ONCODE supported by the Dutch Cancer Society. J.H.J.H. was additionally supported by the National Institute of Health (NIH)/National Institute of Aging (NIA) (AG17242), European Research Council Advanced Grant Dam2Age, and Deutsche Forschungsgemeinschaft (DFG, German Research Foundation—Project-ID 73111208—SFB 829); J.H.J.H. and W.P.V. by Memorabel (ZonMW 733050810), BBoL (NWO-ENW 737.016.015), and the European Joint Programme Rare Diseases (TC-NER RD20-113); and W.P.V. by the Regiodeal Foodvalley (162135) and ADPS Longevity Research Award.

Data submission statement

Raw data files for ribosome profiling and mRNA-seq have been submitted to the NCBI Gene Expression Omnibus (GEO) under accession numbers GSE288421 and GSE288427, respectively.

Conflict of Interest statement

The authors declare that they have no actual or apparent conflict of interest between authorship of this study and any other activities.

AI statement

Generative AI tools (ChatGPT4o / Claude 3.5 Sonnet) were used for minor improvements to grammar and sentence structure, but not for data acquisition or analysis. The authors reviewed and edited AI generated changes and take full responsibility for the content of this publication.

References

1. Schumacher B, Pothof J, Vijg J, Hoeijmakers JHJ. The central role of DNA damage in the ageing process. Nature. 2021 Apr 29;592(7856):695–703.

2. Niedernhofer LJ, Gurkar AU, Wang Y, Vijg J, Hoeijmakers JHJ, Robbins PD. Nuclear Genomic Instability and Aging. Annu Rev Biochem. 2018 June 20;87(1):295–322.

3. Vermeij WP, Hoeijmakers JH, Pothof J. Aging: not all DNA damage is equal. Curr Opin Genet Dev. 2014 June;26:124–130.

4. Gyenis A, Chang J, Demmers JJPG, Bruens ST, Barnhoorn S, Brandt RMC, Baar MP, Raseta M, Derks KWJ, Hoeijmakers JHJ, Pothof J. Genome-wide RNA polymerase stalling shapes the transcriptome during aging. Nat Genet. 2023 Feb;55(2):268–279.

5. Vermeij WP, Dollé MET, Reiling E, Jaarsma D, Payan-Gomez C, Bombardieri CR, Wu H, Roks AJM, Botter SM, van der Eerden BC, Youssef SA, Kuiper RV, Nagarajah B, van Oostrom CT, Brandt RMC, Barnhoorn S, Imholz S, Pennings JLA, de Bruin A, Gyenis Á, Pothof J, Vijg J, van Steeg H, Hoeijmakers JHJ. Restricted diet delays accelerated ageing and genomic stress in DNA-repair-deficient mice. Nature. 2016 15;537(7620):427–431. PMCID: PMC5161687

6. Stoeger T, Grant RA, McQuattie-Pimentel AC, Anekalla KR, Liu SS, Tejedor-Navarro H, Singer BD, Abdala-Valencia H, Schwake M, Tetreault MP, Perlman H, Balch WE, Chandel NS, Ridge KM, Sznajder JI, Morimoto RI, Misharin AV, Budinger GRS, Nunes Amaral LA. Aging is associated with a systemic length-associated transcriptome imbalance. Nat Aging. 2022 Dec 9;2(12):1191–1206.

7. Soheili-Nezhad S, Ibáñez-Solé O, Izeta A, Hoeijmakers JHJ, Stoeger T. Time is ticking faster for long genes in aging. Trends Genet. 2024 Mar;S0168952524000271.

8. Walther DM, Kasturi P, Zheng M, Pinkert S, Vecchi G, Ciryam P, Morimoto RI, Dobson CM, Vendruscolo M, Mann M, Hartl FU. Widespread Proteome Remodeling and Aggregation in Aging C. elegans. Cell. 2015 May;161(4):919–932.

9. Janssens GE, Meinema AC, González J, Wolters JC, Schmidt A, Guryev V, Bischoff R, Wit EC, Veenhoff LM, Heinemann M. Protein biogenesis machinery is a driver of replicative aging in yeast. eLife. 2015 Dec 1;4:e08527. PMCID: PMC4718733

10. Kelmer Sacramento E, Kirkpatrick JM, Mazzetto M, Baumgart M, Bartolome A, Di Sanzo S, Caterino C, Sanguanini M, Papaevgeniou N, Lefaki M, Childs D, Bagnoli S, Terzibasi Tozzini E, Di Fraia D, Romanov N, Sudmant PH, Huber W, Chondrogianni N, Vendruscolo M, Cellerino A, Ori A. Reduced proteasome activity in the aging brain results in ribosome stoichiometry loss and aggregation. Mol Syst Biol [Internet]. 2020 June [cited 2020 July 13];16(6). Available from: https://onlinelibrary.wiley.com/doi/abs/10.15252/msb.20209596

11. Keele GR, Zhang JG, Szpyt J, Korstanje R, Gygi SP, Churchill GA, Schweppe DK. Global and tissue-specific aging effects on murine proteomes. Cell Rep. 2023 July;42(7):112715.

12. Anisimova AS, Alexandrov AI, Makarova NE, Gladyshev VN, Dmitriev SE. Protein synthesis and quality control in aging. Aging. 2018 18;10(12):4269–4288. PMCID: PMC6326689

13. Oh HSH, Rutledge J, Nachun D, Pálovics R, Abiose O, Moran-Losada P, Channappa D, Urey DY, Kim K, Sung YJ, Wang L, Timsina J, Western D, Liu M, Kohlfeld P, Budde J, Wilson EN, Guen Y, Maurer TM, Haney M, Yang AC, He Z, Greicius MD, Andreasson KI, Sathyan S, Weiss EF, Milman S, Barzilai N, Cruchaga C, Wagner AD, Mormino E, Lehallier B, Henderson VW, Longo FM, Montgomery SB, Wyss-

Coray T. Organ aging signatures in the plasma proteome track health and disease. Nature. 2023 Dec 7;624(7990):164–172.

14. Loayza-Puch F, Rooijers K, Buil LCM, Zijlstra J, F. Oude Vrielink J, Lopes R, Ugalde AP, van Breugel P, Hofland I, Wesseling J, van Tellingen O, Bex A, Agami R. Tumour-specific proline vulnerability uncovered by differential ribosome codon reading. Nature. 2016 Feb;530(7591):490–494.

15. Hernández-Ortega K, Garcia-Esparcia P, Gil L, Lucas JJ, Ferrer I. Altered Machinery of Protein Synthesis in Alzheimer's: From the Nucleolus to the Ribosome. Brain Pathol. 2016 Sept;26(5):593–605.

16. Anisimova AS, Meerson MB, Gerashchenko MV, Kulakovskiy IV, Dmitriev SE, Gladyshev VN. Multifaceted deregulation of gene expression and protein synthesis with age. Proc Natl Acad Sci. 2020 July 7;117(27):15581–15590.

17. Stein KC, Morales-Polanco F, van der Lienden J, Rainbolt TK, Frydman J. Ageing exacerbates ribosome pausing to disrupt cotranslational proteostasis. Nature. 2022 Jan 27;601(7894):637–642.

18. Woodward K, Shirokikh NE. Translational control in cell ageing: an update. Biochem Soc Trans. 2021 Dec 17;49(6):2853–2869.

19. Di Fraia D, Marino A, Lee JH, Kelmer Sacramento E, Baumgart M, Bagnoli S, Balla T, Schalk F, Kamrad S, Guan R, Caterino C, Giannuzzi C, Tomaz Da Silva P, Sahu AK, Gut H, Siano G, Tiessen M, Terzibasi-Tozzini E, Fornasiero EF, Gagneur J, Englert C, Patil KR, Correia-Melo C, Nedialkova DD, Frydman J, Cellerino A, Ori A. Altered translation elongation contributes to key hallmarks of aging in the killifish brain. Science. 2025 July 31;389(6759):eadk3079.

20. Li GH, Zhu XQ, Xiao FH, Zhao X, Lv L, Yin FQ, Chang L, Ge MX, Wang Q, Zhao J, Tian C, Li Z, Ruan G, Pang R, Gao J, Ma L, Pan XH, Kong QP. A multi-omics molecular landscape of 30 tissues in aging female rhesus macaques. Nat Methods. 2025 Dec;22(12):2658–2669.

21. Kathjoo MB, Srivastava M. A link between DNA double-strand breaks and regulation of global translation. FEBS J. 2022 June;289(11):3093–3096.

22. Boon NJ, Oliveira RA, Körner PR, Kochavi A, Mertens S, Malka Y, Voogd R, Van Der Horst SEM, Huismans MA, Smabers LP, Draper JM, Wessels LFA, Haahr P, Roodhart JML, Schumacher TNM, Snippert HJ, Agami R, Brummelkamp TR. DNA damage induces p53-independent apoptosis through ribosome stalling. Science. 2024 May 17;384(6697):785–792.

23. Bournique E, Sanchez A, Oh S, Ghazarian D, Mahieu AL, Manjunath L, Ednacot E, Ortega P, Masri S, Marazzi I, Buisson R. ATM and IRAK1 orchestrate two distinct mechanisms of NF-κB activation in response to DNA damage. Nat Struct Mol Biol. 2025 Apr;32(4):740–755.

24. Vermeij WP, Hoeijmakers JHJ, Pothof J. Genome Integrity in Aging: Human Syndromes, Mouse Models, and Therapeutic Options. Annu Rev Pharmacol Toxicol. 2016 Jan 6;56(1):427–445.

25. Perez K, Parras A, Picó S, Rechsteiner C, Haghani A, Brooke R, Mrabti C, Schoenfeldt L, Horvath S, Ocampo A. DNA repair-deficient premature aging models display accelerated epigenetic age. Aging Cell. 2024 Feb;23(2):e14058.

26. Weeda G, Donker I, De Wit J, Morreau H, Janssens R, Vissers CJ, Nigg A, Van Steeg H, Bootsma D, Hoeijmakers JHJ. Disruption of mouse ERCC1 results in a novel repair syndrome with growth failure, nuclear abnormalities and senescence. Curr Biol. 1997 June;7(6):427–439.

27. Dollé MET, Kuiper RV, Roodbergen M, Robinson J, de Vlugt S, Wijnhoven SWP, Beems RB, de la Fonteyne L, de With P, van der Pluijm I, Niedernhofer LJ, Hasty P, Vijg J, Hoeijmakers JHJ, van Steeg H. Broad segmental progeroid changes in short-lived *Ercc1* $^{-/\Delta 7}$ mice. Pathobiol Aging Age-Relat Dis. 2011 Jan;1(1):7219.

28. White RR, Milholland B, MacRae SL, Lin M, Zheng D, Vijg J. Comprehensive transcriptional landscape of aging mouse liver. BMC Genomics. 2015 Dec;16(1):899.

29. Gregg SQ, Gutiérrez V, Rasile Robinson A, Woodell T, Nakao A, Ross MA, Michalopoulos GK, Rigatti L, Rothermel CE, Kamileri I, Garinis GA, Beer Stolz D, Niedernhofer LJ. A mouse model of accelerated liver aging caused by a defect in DNA repair. Hepatology. 2012 Feb;55(2):609–621.

30. Chen L, Ma MY, Sun M, Jiang LY, Zhao XT, Fang XX, Man Lam S, Shui GH, Luo J, Shi XJ, Song BL. Endogenous sterol intermediates of the mevalonate pathway regulate HMGCR degradation and SREBP-2 processing. J Lipid Res. 2019 Oct;60(10):1765–1775.

31. Klaassen CD, Aleksunes LM. Xenobiotic, Bile Acid, and Cholesterol Transporters: Function and Regulation. Pharmacol Rev. 2010 Mar;62(1):1–96.

32. Ponsuksili S, Murani E, Brand B, Schwerin M, Wimmers K. Integrating expression profiling and whole-genome association for dissection of fat traits in a porcine model. J Lipid Res. 2011 Apr;52(4):668–678.

33. Zhao Y, Simon M, Seluanov A, Gorbunova V. DNA damage and repair in age-related inflammation. Nat Rev Immunol. 2023 Feb;23(2):75–89.

34. Gulhar R, Ashraf MA, Jialal I. Physiology, Acute Phase Reactants. StatPearls [Internet]. Treasure Island (FL): StatPearls Publishing; 2023 [cited 2024 Jan 9]. Available from: http://www.ncbi.nlm.nih.gov/books/NBK519570/ PMID: 30137854

35. Liu Q, Shvarts T, Sliz P, Gregory RI. RiboToolkit: an integrated platform for analysis and annotation of ribosome profiling data to decode mRNA translation at codon resolution. Nucleic Acids Res. 2020 July 2;48(W1):W218–W229.

36. Khitun A, Ness TJ, Slavoff SA. Small open reading frames and cellular stress responses. Mol Omics. 2019;15(2):108–116.

37. Young SK, Wek RC. Upstream Open Reading Frames Differentially Regulate Gene-specific Translation in the Integrated Stress Response. J Biol Chem. 2016 Aug;291(33):16927–16935.

38. Barbosa C, Peixeiro I, Romão L. Gene Expression Regulation by Upstream Open Reading Frames and Human Disease. Fisher EMC, editor. PLoS Genet. 2013 Aug 8;9(8):e1003529.

39. Chen HH, Tarn WY. uORF-mediated translational control: recently elucidated mechanisms and implications in cancer. RNA Biol. 2019 Oct 3;16(10):1327–1338.

40. Silva J, Fernandes R, Romão L. Translational Regulation by Upstream Open Reading Frames and Human Diseases. In: Romão L, editor. MRNA Metab Hum Dis [Internet]. Cham: Springer International Publishing; 2019 [cited 2023 June 30]. p. 99–116. Available from: http://link.springer.com/10.1007/978-3-030-19966-1_5

41. Johnstone TG, Bazzini AA, Giraldez AJ. Upstream ORF s are prevalent translational repressors in vertebrates. EMBO J. 2016 Apr;35(7):706–723.

42. Sung B, Park S, Yu BP, Chung HY. Modulation of PPAR in Aging, Inflammation, and Calorie Restriction. J Gerontol A Biol Sci Med Sci. 2004 Oct 1;59(10):B997–B1006.

43. Nevedomskaya E, Meissner A, Goraler S, De Waard M, Ridwan Y, Zondag G, Van Der Pluijm I, Deelder AM, Mayboroda OA. Metabolic Profiling of Accelerated Aging ERCC1$^{d/-}$ Mice. J Proteome Res. 2010 July 2;9(7):3680–3687.

44. Czerwińska J, Nowak M, Wojtczak P, Dziuban-Lech D, Cieśla JM, Kołata D, Gajewska B, Barańczyk-Kuźma A, Robinson AR, Shane HL, Gregg SQ, Rigatti LH, Yousefzadeh MJ, Gurkar AU, McGowan SJ, Kosicki K, Bednarek M, Zarakowska E, Gackowski D, Oliński R, Speina E, Niedernhofer LJ, Tudek B. ERCC1-deficient cells and mice are hypersensitive to lipid peroxidation. Free Radic Biol Med. 2018 Aug;124:79–96.

45. Huang J, Tabbi-Anneni I, Gunda V, Wang L. Transcription factor Nrf2 regulates SHP and lipogenic gene expression in hepatic lipid metabolism. Am J Physiol Gastrointest Liver Physiol. 2010 Dec;299(6):G1211-1221. PMCID: PMC3006243

46. Im SS, Yousef L, Blaschitz C, Liu JZ, Edwards RA, Young SG, Raffatellu M, Osborne TF. Linking Lipid Metabolism to the Innate Immune Response in Macrophages through Sterol Regulatory Element Binding Protein-1a. Cell Metab. 2011 May;13(5):540–549.

47. Schumacher B, van der Pluijm I, Moorhouse MJ, Kosteas T, Robinson AR, Suh Y, Breit TM, van Steeg H, Niedernhofer LJ, van Ijcken W, Bartke A, Spindler SR, Hoeijmakers JHJ, van der Horst GTJ, Garinis GA. Delayed and accelerated aging share common longevity assurance mechanisms. PLoS Genet. United States; 2008 Aug 15;4(8):e1000161. PMCID: PMC2493043

48. Wilson KA, Chamoli M, Hilsabeck TA, Pandey M, Bansal S, Chawla G, Kapahi P. Evaluating the beneficial effects of dietary restrictions: A framework for precision nutrigeroscience. Cell Metab. 2021 Nov;33(11):2142–2173.

49. Rasa SMM, Annunziata F, Krepelova A, Nunna S, Omrani O, Gebert N, Adam L, Käppel S, Höhn S, Donati G, Jurkowski TP, Rudolph KL, Ori A, Neri F. Inflammaging is driven by upregulation of innate immune receptors and systemic interferon signaling and is ameliorated by dietary restriction. Cell Rep. 2022 June;39(13):111017.

50. Yang H, Zingaro VA, Lincoff J, Tom H, Oikawa S, Oses-Prieto JA, Edmondson Q, Seiple I, Shah H, Kajimura S, Burlingame AL, Grabe M, Ruggero D. Remodelling of the translatome controls diet and its impact on tumorigenesis. Nature [Internet]. 2024 Aug 14 [cited 2024 Sept 2]; Available from: https://www.nature.com/articles/s41586-024-07781-7

51. Todisco S, Santarsiero A, Convertini P, De Stefano G, Gilio M, Iacobazzi V, Infantino V. PPAR Alpha as a Metabolic Modulator of the Liver: Role in the Pathogenesis of Nonalcoholic Steatohepatitis (NASH). Biology. 2022 May 23;11(5):792.

52. He Y, Yang W, Huang L, Mever MA, Ramautar R, Harms A, Rijksen Y, Brandt RMC, Barnhoorn S, Smit K, Jaarsma D, Lindenburg P, Hoeijmakers JHJ, Vermeij WP, Hankemeier T. Metabolomic analysis of dietary-restriction-induced attenuation of sarcopenia in prematurely aging DNA repair-deficient mice. J Cachexia Sarcopenia Muscle. 2024 June;15(3):868–882.

53. Xu AF, Molinuevo R, Fazzari E, Tom H, Zhang Z, Menendez J, Casey KM, Ruggero D, Hinck L, Pritchard JK, Barna M. Subfunctionalized expression drives evolutionary retention of ribosomal protein paralogs Rps27 and Rps27l in vertebrates. eLife. 2023 June 12;12:e78695.

54. Lopes I, Altab G, Raina P, De Magalhães JP. Gene Size Matters: An Analysis of Gene Length in the Human Genome. Front Genet. 2021 Feb 11;12:559998.

55. Ibañez-Solé O, Barrio I, Izeta A. Age or lifestyle-induced accumulation of genotoxicity is associated with a length-dependent decrease in gene expression. iScience. 2023 Apr;26(4):106368.

56. Moshage H. Cytokines and the hepatic acute phase response. J Pathol. 1997 Mar;181(3):257–266.

57. Porukala M, Vinod PK. Network-level analysis of ageing and its relationship with diseases and tissue regeneration in the mouse liver. Sci Rep. 2023 Mar 21;13(1):4632.

58. Cohen I, Rider P, Vornov E, Tomas M, Tudor C, Wegner M, Brondani L, Freudenberg M, Mittler G, Ferrando-May E, Dinarello CA, Apte RN, Schneider R. IL-1α is a DNA damage sensor linking genotoxic stress signaling to sterile inflammation and innate immunity. Sci Rep. 2015 Oct 6;5(1):14756.

59. Härtlova A, Erttmann SF, Raffi FAm, Schmalz AM, Resch U, Anugula S, Lienenklaus S, Nilsson LM, Kröger A, Nilsson JA, Ek T, Weiss S, Gekara NO. DNA Damage Primes the Type I Interferon System via the Cytosolic DNA Sensor STING to Promote Anti-Microbial Innate Immunity. Immunity. 2015 Feb;42(2):332–343.

60. Gulen MF, Samson N, Keller A, Schwabenland M, Liu C, Glück S, Thacker VV, Favre L, Mangeat B, Kroese LJ, Krimpenfort P, Prinz M, Ablasser A. cGAS–STING drives ageing-related inflammation and neurodegeneration. Nature. 2023 Aug 10;620(7973):374–380.

61. Bock KW. Functions of aryl hydrocarbon receptor (AHR) and CD38 in NAD metabolism and nonalcoholic steatohepatitis (NASH). Biochem Pharmacol. 2019 Nov;169:113620.

62. Bock KW. Aryl hydrocarbon receptor (AHR) functions in infectious and sterile inflammation and NAD+-dependent metabolic adaptation. Arch Toxicol. 2021 Nov;95(11):3449–3458.

63. Birkisdóttir MB, van Galen I, Brandt RMC, Barnhoorn S, van Vliet N, van Dijk C, Nagarajah B, Imholz S, van Oostrom CT, Reiling E, Gyenis Á, Mastroberardino PG, Jaarsma D, van Steeg H, Hoeijmakers JHJ, Dollé MET, Vermeij WP. The use of progeroid DNA repair-deficient mice for assessing anti-aging compounds, illustrating the benefits of nicotinamide riboside. Front Aging. Switzerland; 2022;3:1005322. PMCID: PMC9596940

64. Hou Y, Lautrup S, Cordonnier S, Wang Y, Croteau DL, Zavala E, Zhang Y, Moritoh K, O'Connell JF, Baptiste BA, Stevnsner TV, Mattson MP, Bohr VA. NAD(+) supplementation normalizes key Alzheimer's features and DNA damage responses in a new AD mouse model with introduced DNA repair deficiency. Proc Natl Acad Sci U S A. United States; 2018 Feb 20;115(8):E1876–E1885. PMCID: PMC5828618

65. Scheibye-Knudsen M, Mitchell SJ, Fang EF, Iyama T, Ward T, Wang J, Dunn CA, Singh N, Veith S, Hasan-Olive MM, Mangerich A, Wilson MA, Mattson MP, Bergersen LH, Cogger VC, Warren A, Le Couteur DG, Moaddel R, Wilson DM 3rd, Croteau DL, de Cabo R, Bohr VA. A high-fat diet and NAD(+) activate Sirt1 to rescue premature aging in cockayne syndrome. Cell Metab. United States; 2014 Nov 4;20(5):840–855. PMCID: PMC4261735

66. Kane A, Chellappa K, Schultz M, Diener C, Gibbons S, Baur J, Rajman L, Sinclair D. LONG-TERM NMN TREATMENT INCREASES LIFESPAN AND HEALTHSPAN IN MICE IN A SEX DEPENDENT MANNER. Innov Aging. 2023 Dec 21;7(Supplement_1):1077–1077.

67. Fang EF, Hou Y, Lautrup S, Jensen MB, Yang B, SenGupta T, Caponio D, Khezri R, Demarest TG, Aman Y, Figueroa D, Morevati M, Lee HJ, Kato H, Kassahun H, Lee JH, Filippelli D, Okur MN, Mangerich A, Croteau DL, Maezawa Y, Lyssiotis CA, Tao J, Yokote K, Rusten TE, Mattson MP, Jasper H, Nilsen H, Bohr VA. NAD+ augmentation restores mitophagy and limits accelerated aging in Werner syndrome. Nat Commun. 2019 21;10(1):5284. PMCID: PMC6872719

68. Wek RC. Role of eIF2α Kinases in Translational Control and Adaptation to Cellular Stress. Cold Spring Harb Perspect Biol. 2018 July;10(7):a032870.

69. Dennis MD, Jefferson LS, Kimball SR. Role of p70S6K1-mediated Phosphorylation of eIF4B and PDCD4 Proteins in the Regulation of Protein Synthesis. J Biol Chem. 2012 Dec;287(51):42890–42899.

70. Zhang D, Zhou Y, Ma Y, Jiang P, Lv H, Liu S, Mu Y, Zhou C, Xiao S, Ji G, Liu P, Zhang N, Sun D, Sun H, Wu N, Jin Y. Ribosomal protein L22-like1 (RPL22L1) mediates sorafenib sensitivity via ERK in hepatocellular carcinoma. Cell Death Discov. 2022 Aug 17;8(1):365.

71. Zhang Y, O'Leary MN, Peri S, Wang M, Zha J, Melov S, Kappes DJ, Feng Q, Rhodes J, Amieux PS, Morris DR, Kennedy BK, Wiest DL. Ribosomal Proteins Rpl22 and Rpl22l1 Control Morphogenesis by Regulating Pre-mRNA Splicing. Cell Rep. 2017 Jan;18(2):545–556.

72. Wu N, Wei J, Wang Y, Yan J, Qin Y, Tong D, Pang B, Sun D, Sun H, Yu Y, Sun W, Meng X, Zhang C, Bai J, Chen F, Geng J, Lee KY, Fu S, Jin Y. Ribosomal L22-like1 (RPL22L1) Promotes Ovarian Cancer Metastasis by Inducing Epithelial-to-Mesenchymal Transition. Guan XY, editor. PLOS ONE. 2015 Nov 30;10(11):e0143659.

73. Xiong X, Zhao Y, Tang F, Wei D, Thomas D, Wang X, Liu Y, Zheng P, Sun Y. Ribosomal protein S27-like is a physiological regulator of p53 that suppresses genomic instability and tumorigenesis. eLife. 2014 Aug 21;3:e02236.

74. Xiong X, Liu X, Li H, He H, Sun Y, Zhao Y. Ribosomal protein S27-like regulates autophagy via the β-TrCP-DEPTOR-mTORC1 axis. Cell Death Dis. 2018 Nov 13;9(11):1131.

75. Hountondji C, Bulygin K, Créchet JB, Woisard A, Tuffery P, Nakayama J ichi, Frolova L, Knud H N, Karpova G, Baouz S. The CCA-end of P-tRNA Contacts Both the Human RPL36AL and the A-site Bound Translation Termination Factor eRF1 at the Peptidyl Transferase Center of the Human 80S Ribosome. Open Biochem J. 2014 Aug 5;8(1):52–67.

76. Barger JL, Anderson RM, Newton MA, Da Silva C, Vann JA, Pugh TD, Someya S, Prolla TA, Weindruch R. A Conserved Transcriptional Signature of Delayed Aging and Reduced Disease Vulnerability Is Partially Mediated by SIRT3. Vina J, editor. PLOS ONE. 2015 Apr 1;10(4):e0120738.

77. Gonskikh Y, Polacek N. Alterations of the translation apparatus during aging and stress response. Mech Ageing Dev. 2017 Dec;168:30–36.

78. Folgueras AR, Freitas-Rodríguez S, Velasco G, López-Otín C. Mouse Models to Disentangle the Hallmarks of Human Aging. Circ Res. 2018 Sept 14;123(7):905–924.

79. Di Fraia D, Marino A, Lee JH, Kelmer Sacramento E, Baumgart M, Bagnoli S, Tomaz da Silva P, Kumar Sahu A, Siano G, Tiessen M, Terzibasi-Tozzini E, Gagneur J, Frydman J, Cellerino A, Ori A. Impaired biogenesis of basic proteins impacts multiple hallmarks of the aging brain. BioRxiv Prepr Serv Biol. 2024 Jan 9;2023.07.20.549210. PMCID: PMC10802395

80. Godet AC, David F, Hantelys F, Tatin F, Lacazette E, Garmy-Susini B, Prats AC. IRES Trans-Acting Factors, Key Actors of the Stress Response. Int J Mol Sci. 2019 Feb 20;20(4):924.

81. Santinha D, Vilaça A, Estronca L, Schüler SC, Bartoli C, De Sandre-Giovannoli A, Figueiredo A, Quaas M, Pompe T, Ori A, Ferreira L. Remodeling of the Cardiac Extracellular Matrix Proteome During Chronological and Pathological Aging. Mol Cell Proteomics. 2024 Jan;23(1):100706.

82. Niedernhofer LJ, Garinis GA, Raams A, Lalai AS, Robinson AR, Appeldoorn E, Odijk H, Oostendorp R, Ahmad A, van Leeuwen W, Theil AF, Vermeulen W, van der Horst GTJ, Meinecke P, Kleijer WJ, Vijg J, Jaspers NGJ, Hoeijmakers JHJ. A new progeroid syndrome reveals that genotoxic stress suppresses the somatotroph axis. Nature. England; 2006 Dec 21;444(7122):1038–1043. PMID: 17183314

83. Van Der Linden J, Stefens SJM, Heredia-Genestar JM, Ridwan Y, Brandt RMC, Van Vliet N, De Beer I, Van Thiel BS, Steen H, Cheng C, Roks AJM, Danser AHJ, Essers J, Van Der Pluijm I. Ercc1 DNA repair deficiency results in vascular aging characterized by VSMC phenotype switching, ECM remodeling, and an increased stress response. Aging Cell. 2024 May;23(5):e14126.

84. Paine PT, Rechsteiner C, Morandini F, Desdín-Micó G, Mrabti C, Parras A, Haghani A, Brooke R, Horvath S, Seluanov A, Gorbunova V, Ocampo A. Initiation phase cellular reprogramming ameliorates DNA damage in the ERCC1 mouse model of premature aging. Front Aging. 2024 Jan 23;4:1323194.

85. Perez K, Parras A, Picó S, Rechsteiner C, Haghani A, Brooke R, Mrabti C, Schoenfeldt L, Horvath S, Ocampo A. DNA repair-deficient premature aging models display accelerated epigenetic age. Aging Cell. 2024 Feb;23(2):e14058.

86. Vanhooren V, Dewaele S, Libert C, Engelborghs S, De Deyn PP, Toussaint O, Debacq-Chainiaux F, Poulain M, Glupczynski Y, Franceschi C, Jaspers K, Van Der Pluijm I, Hoeijmakers J, Chen CC. Serum N-glycan profile shift during human ageing. Exp Gerontol. 2010 Oct;45(10):738–743.

87. Wei YN, Hu HY, Xie GC, Fu N, Ning ZB, Zeng R, Khaitovich P. Transcript and protein expression decoupling reveals RNA binding proteins and miRNAs as potential modulators of human aging. Genome Biol. 2015 Dec;16(1):41.

88. Khatir I, Brunet MA, Meller A, Amiot F, Patel T, Lapointe X, Avila Lopez J, Guilloy N, Castonguay A, Husain MA, Germain JSt, Boisvert FM, Plourde M, Roucou X, Laurent B. Decoupling of mRNA and Protein Expression in Aging Brains Reveals the Age-Dependent Adaptation of Specific Gene Subsets. Cells. 2023 Feb 14;12(4):615.

89. Ishikawa K. Multilayered regulation of proteome stoichiometry. Curr Genet. 2021 Dec;67(6):883–890.

90. Mueller S, Wahlander A, Selevsek N, Otto C, Ngwa EM, Poljak K, Frey AD, Aebi M, Gauss R. Protein degradation corrects for imbalanced subunit stoichiometry in OST complex assembly. Gilmore R, editor. Mol Biol Cell. 2015 July 5;26(14):2596–2608.

91. Kovács D, Biró JB, Ahmed S, Kovács M, Sigmond T, Hotzi B, Varga M, Vincze VV, Mohammad U, Vellai T, Barna J. Age-dependent heat shock hormesis to HSF -1 deficiency suggests a compensatory mechanism mediated by the unfolded protein response and innate immunity in young *Caenorhabditis elegans*. Aging Cell. 2024 Oct;23(10):e14246.

92. Cordes J, Zhao S, Engel CM, Stingele J. Cellular responses to RNA damage. Cell. 2025 Feb;188(4):885–900.

93. Zaher HS, Mosammaparast N. RNA Damage Responses in Cellular Homeostasis, Genome Stability, and Disease. Annu Rev Pathol Mech Dis. 2025 Jan 24;20(1):433–457.

94. Tsao N, Lombardi PM, Park A, Olabode J, Rodell R, Sun H, Padmanaban S, Brickner JR, Tsai MS, Pollina EA, Chen CK, Mosammaparast N. YTHDC1 cooperates with the THO complex to prevent RNA-damage-induced DNA breaks. Mol Cell. 2025 Mar;85(6):1085-1100.e9.

95. McGlincy NJ, Ingolia NT. Transcriptome-wide measurement of translation by ribosome profiling. Methods San Diego Calif. 2017 15;126:112–129. PMCID: PMC5582988

96. Palomar-Siles M, Heldin A, Zhang M, Strandgren C, Yurevych V, Van Dinter JT, Engels SAG, Hofman DA, Öhlin S, Meineke B, Bykov VJN, Van Heesch S, Wiman KG. Translational readthrough of nonsense mutant TP53 by mRNA incorporation of 5-Fluorouridine. Cell Death Dis. 2022 Nov 25;13(11):997.

97. Langmead B, Salzberg SL. Fast gapped-read alignment with Bowtie 2. Nat Methods. 2012 Apr;9(4):357–359.

98. Lorenzo Calviello, Dominique Sydow, Dermot Harnett, Uwe Ohler. Ribo-seQC: comprehensive analysis of cytoplasmic and organellar ribosome profiling data. bioRxiv. 2019 Jan 1;601468.

99. Martin M. Cutadapt removes adapter sequences from high-throughput sequencing reads. EMBnet.journal. 2011 May 2;17(1):10.

100. Calviello L, Hirsekorn A, Ohler U. Quantification of translation uncovers the functions of the alternative transcriptome. Nat Struct Mol Biol. 2020 Aug;27(8):717–725.

101. Robinson JT, Thorvaldsdóttir H, Winckler W, Guttman M, Lander ES, Getz G, Mesirov JP. Integrative genomics viewer. Nat Biotechnol. 2011 Jan;29(1):24–26.

102. Subramanian A, Tamayo P, Mootha VK, Mukherjee S, Ebert BL, Gillette MA, Paulovich A, Pomeroy SL, Golub TR, Lander ES, Mesirov JP. Gene set enrichment analysis: A knowledge-based approach for interpreting genome-wide expression profiles. Proc Natl Acad Sci. 2005 Oct 25;102(43):15545–15550.

103. Chothani S, Adami E, Ouyang JF, Viswanathan S, Hubner N, Cook SA, Schafer S, Rackham OJL. deltaTE: Detection of Translationally Regulated Genes by Integrative Analysis of Ribo-seq and RNA-seq Data. Curr Protoc Mol Biol [Internet]. 2019 Dec [cited 2022 Nov 15];129(1). Available from: https://onlinelibrary.wiley.com/doi/10.1002/cpmb.108

104. Kumari R, Michel AM, Baranov PV. PausePred and Rfeet: webtools for inferring ribosome pauses and visualizing footprint density from ribosome profiling data. RNA. 2018 Oct;24(10):1297–1304.

105. Zhou Q, Chipperfield H, Melton DA, Wong WH. A gene regulatory network in mouse embryonic stem cells. Proc Natl Acad Sci. 2007 Oct 16;104(42):16438–16443.

Figure 1. Ribosome profiling of *Ercc1*$^{\Delta/-}$ liver results in clear separation between groups. (**A**) Schematic representation of experimental set-up and tissue acquisition from male wild-type and *Ercc1*$^{\Delta/-}$ mice under AL and DR conditions; WT_AL (gray); WT_DR (green); Ercc1_AL (Blue); and Ercc1_DR (red). Food was provided to the animals just before the start of the dark (active) period, Zeitgeber Time (ZT) 12:00, except for the day of sacrifice, when no food was given prior to collect between ZT13 and ZT16. (**B**) Footprint length distribution compared to total reads. (**C**) Quantification of RNA contaminants. Reads that were not tRNA or rRNA were considered "clean". (**D**) Gene meta-analysis of p-site specific frame preference between Transcription Start Site (TSS) and Transcription End Site (TES). (**E**) Quantification of p-site frame preference indicative of footprint periodicity. (**F-G**) PCA plots with 95% confidence intervals for mRNA- (F) and Ribo-seq (G). Values are mean ± SD.

Figure 2. Pathway analysis changes in *Ercc1*$^{\Delta/-}$ mice at the transcriptional and translational level. (**A**) Scatter plot of gene expression (n=1533) in *Ercc1*$^{\Delta/-}$ mice, comparing transcriptional (mRNA-seq) and translational (Ribo-seq) levels. Forwarded genes have a significant change in mRNA and ribosome-protected fragments (RPF) at the same rate, with no significant change in translational efficiency (TE). Exclusive genes are regulated only at the translational level, intensified genes have a significant change in TE that acts with the effect of transcription, and buffered genes have a significant change in TE that counteracts the change in RNA. (**B-E**) Upstream regulator (B-C) and signaling pathway (D-E) analysis based on differentially expressed genes in AL-fed *Ercc1*$^{\Delta/-}$ mice compared to WT at the mRNA (B,D) and Ribo-seq (C,E) level. Numerical parameters of pathways and upstream regulators were calculated with Ingenuity Pathway Analysis (IPA) and subsidiary pathways were collapsed if top parent pathways were present. Red means upregulated, white indicates pathways with z-scores near zero or those ineligible due to a limited number of hits, blue means downregulated, and gray means that no activity prediction could be made for this pathway.

Figure 3. ERCC1-deficiency-driven modifications in translational dynamics and uORF expression. (**A-B**) GSEA enrichment graphs of translation initiation factors (A) and cytosolic ribosomal subunits (B), based on ribosome profiling data (**C-D**) Violin plots depicting the max pause score intensity (C) and the mean number of pause sites found per gene transcript averaged per group (D). Highlighted intensity values represent median intensity. (**E-F**) Bar graph plot showing absolute (E) and normalized (F) P-site codon occupancy log2 fold changes in *Ercc1*$^{\Delta/-}$ as compared to WT with essential amino acids being indicated in red and error bars depicting SD. (**G**) Simplified graphical representation of the regulatory function of (overlapping) upstream open reading frames (uORFs) on a transcript's canonical ORF. (**H**) Vulcano plot of (overlapping) uORF expression in *Ercc1*$^{\Delta/-}$_AL as compared to WT_AL with differentially regulated uORFs being indicated in black. (**I**) Scatterplot illustrating the relation between uORF and canonical fold change differences in *Ercc1*$^{\Delta/-}$_AL vs WT_AL with significantly altered uORFs being depicted in black. A regression line with 95% confidence interval, based on the significant uORFs, is represented in red. (**J**) Pie chart depicting the number of uORFs that are more strongly up or down regulated than the canonical ORF they belong to in *Ercc1*$^{\Delta/-}$_AL as compared to WT_AL. (**K**) Venn diagram of the overlapping differentially regulated uORFs in *Ercc1*$^{\Delta/-}$_AL and 104-week-old WT_AL compared to young 16-week-old WT_AL mice. Arrows indicate activation or inhibition of uORF expression. Significance levels are denoted 'ns' for $p>0.05$ and *** for $p\leq0.001$, with comparisons made to indicated control groups.

Figure 4. Effect of DR on gene and pathways expression in the liver of *Ercc1*$^{\Delta/-}$ mice. (**A**) Scatter plot of gene expression(n=986) in DR-fed vs AL-fed *Ercc1*$^{\Delta/-}$ mice, comparing transcriptional (mRNA-seq) and translational (Ribo-seq) levels. Forwarded genes have a significant change in mRNA and RPF at the same rate, with no significant change in translational efficiency (TE). Exclusive genes are regulated only at the translational level and buffered genes have a significant change in TE that counteracts the change in RNA. (**B-C**) Venn diagram of the DEGs and their overlap due to DR in *Ercc1*$^{\Delta/-}$ and WT mice as compared to AL-fed controls (B). Scatter plot of the overlapping DEGs divided between concordant and discordant expression (C). (**D-E**) Venn diagram of the DEGs caused by the *Ercc1*$^{\Delta/-}$ mutation, the effect of DR in *Ercc1*$^{\Delta/-}$ and their overlap (D). Scatter plot of the overlapping DEGs divided between concordant and discordant expression (E). (**F**) Upstream regulator analysis of ribosome profiling based differentially expressed genes in DR vs AL-fed *Ercc1*$^{\Delta/-}$ mice level. (**G-H**) Signaling pathways altered due to DR in *Ercc1*$^{\Delta/-}$ (G) and WT (H) genotypical background. Numerical parameters of pathways and upstream regulators were calculated with Ingenuity Pathway Analysis (IPA). Red means upregulated, white indicates pathways with z-scores near zero or those ineligible due to a limited number of hits, blue means downregulated, and gray means that an activity prediction could not be calculated for this pathway.

Figure 5. DR modulates translation dynamics in *Ercc1*$^{\Delta/-}$ mice distinctly from WT mice. (**A-B**) Heatmaps of ribosome profiling expression data for initiation factors (A) and cytosolic ribosomal subunits (B) with red indicating an upregulation and blue a downregulation. Relevant factors are highlighted. (**C-E**) Vulcano plots of cytosolic ribosomal subunit expression in ribosome profiling data for the effect of *Ercc1*$^{\Delta/-}$ against WT (C), the effect of DR in *Ercc1*$^{\Delta/-}$ against AL-fed WT mice (D), and the effect of DR in *Ercc1*$^{\Delta/-}$ against AL-fed *Ercc1*$^{\Delta/-}$ (E). Relevant factors are highlighted. (**F-G**) Violin plots displaying the mean number (F) and median intensity (G) of ribosomal pause site scores averaged per group. (**H-I**) Bar graph plot showing log2 fold changes of absolute (H) and aa normalized (I) p-site codon occupancy in DR-fed *Ercc1*$^{\Delta/-}$ mice compared to AL-fed *Ercc1*$^{\Delta/-}$. Essential amino acids are indicated in red. Error bars depict SD. Significance levels are denoted 'ns' for $p>0.05$, **$p\leq0.01$, and **** for $p\leq0.0001$, with comparisons made to indicated control groups.

Figure 6. Effects of DR on upstream open reading frames. (**A**) Bar graph displaying the number of differentially expressed uORFs and overlapping uORFs in *Ercc1*$^{\Delta/-}$ AL or DR-fed and WT DR-fed against WT AL-fed mice. (**B**) Vulcano plot of uORF expression altered by DR in *Ercc1*$^{\Delta/-}$. Black dots are significant while gray dots are not. (**C**) Venn diagram of differentially expressed uORFs due to DR in WT and *Ercc1*$^{\Delta/-}$ genetic backgrounds. Arrows indicate activation or inhibition of uORF sequence translation. (**D**) Scatterplot illustrating the relation between uORF and canonical fold change differences between DR and AL-fed *Ercc1*$^{\Delta/-}$ mice with significantly altered uORFs being depicted in black. A regression line with 95% confidence interval, based on the significant uORFs, is represented in red. (**E**) Heatmap representing the relative ratio between uORF and canonical ORF expression based on all uORFs that were differentially regulated between WT_AL and at least one other group. Red means upregulated, blue means downregulated, and gray means that no direction could be calculated.

Figure 1

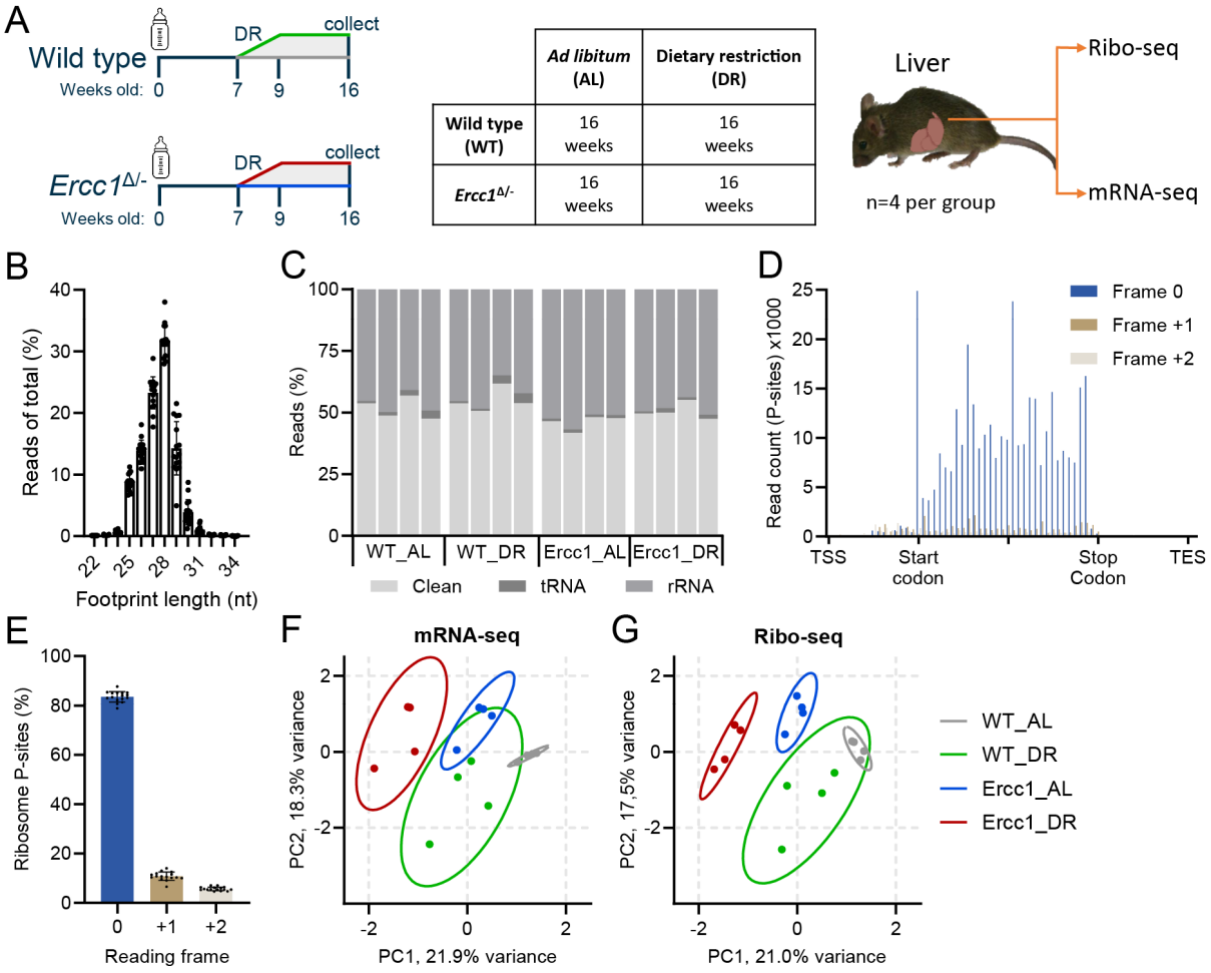
A
Wild type
Weeks old: 0 7 9 16
DR
collect
Ercc1Δ/-
Weeks old: 0 7 9 16
DR
collect
Ad libitum (AL)
Dietary restriction (DR)
Wild type (WT)
16 weeks
16 weeks
Ercc1Δ/-
16 weeks
16 weeks
Liver
Ribo-seq
mRNA-seq
n=4 per group
B
Reads of total (%)
Footprint length (nt)
C
Reads (%)
WT_AL
WT_DR
Ercc1_AL
Ercc1_DR
Clean
tRNA
rRNA
D
Read count (P-sites) x1000
Frame 0
Frame +1
Frame +2
TSS
Start codon
Stop Codon
TES
E
Ribosome P-sites (%)
Reading frame
F
mRNA-seq
PC2, 18.3% variance
PC1, 21.9% variance
G
Ribo-seq
PC2, 17,5% variance
PC1, 21.0% variance
WT_AL
WT_DR
Ercc1_AL
Ercc1_DR

Figure2

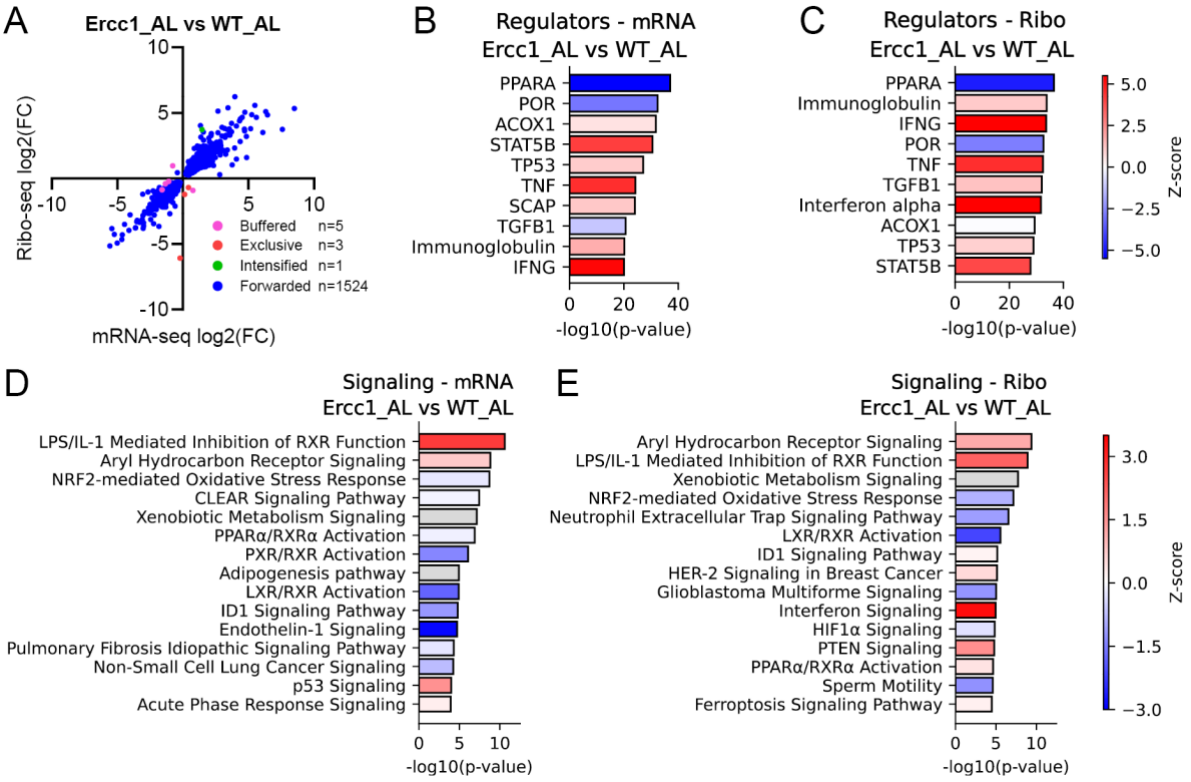
A
Ercc1_AL vs WT_AL
Ribo-seq log2(FC)
mRNA-seq log2(FC)
Buffered n=5
Exclusive n=3
Intensified n=1
Forwarded n=1524
B
Regulators - mRNA
Ercc1_AL vs WT_AL
PPARA
POR
ACOX1
STAT5B
TP53
TNF
SCAP
TGFB1
Immunoglobulin
IFNG
-log10(p-value)
C
Regulators - Ribo
Ercc1_AL vs WT_AL
PPARA
Immunoglobulin
IFNG
POR
TNF
TGFB1
Interferon alpha
ACOX1
TP53
STAT5B
-log10(p-value)
Z-score
D
Signaling - mRNA
Ercc1_AL vs WT_AL
LPS/IL-1 Mediated Inhibition of RXR Function
Aryl Hydrocarbon Receptor Signaling
NRF2-mediated Oxidative Stress Response
CLEAR Signaling Pathway
Xenobiotic Metabolism Signaling
PPARα/RXRα Activation
PXR/RXR Activation
Adipogenesis pathway
LXR/RXR Activation
ID1 Signaling Pathway
Endothelin-1 Signaling
Pulmonary Fibrosis Idiopathic Signaling Pathway
Non-Small Cell Lung Cancer Signaling
p53 Signaling
Acute Phase Response Signaling
-log10(p-value)
E
Signaling - Ribo
Ercc1_AL vs WT_AL
Aryl Hydrocarbon Receptor Signaling
LPS/IL-1 Mediated Inhibition of RXR Function
Xenobiotic Metabolism Signaling
NRF2-mediated Oxidative Stress Response
Neutrophil Extracellular Trap Signaling Pathway
LXR/RXR Activation
ID1 Signaling Pathway
HER-2 Signaling in Breast Cancer
Glioblastoma Multiforme Signaling
Interferon Signaling
HIF1α Signaling
PTEN Signaling
PPARα/RXRα Activation
Sperm Motility
Ferroptosis Signaling Pathway
-log10(p-value)
Z-score

Figure 3

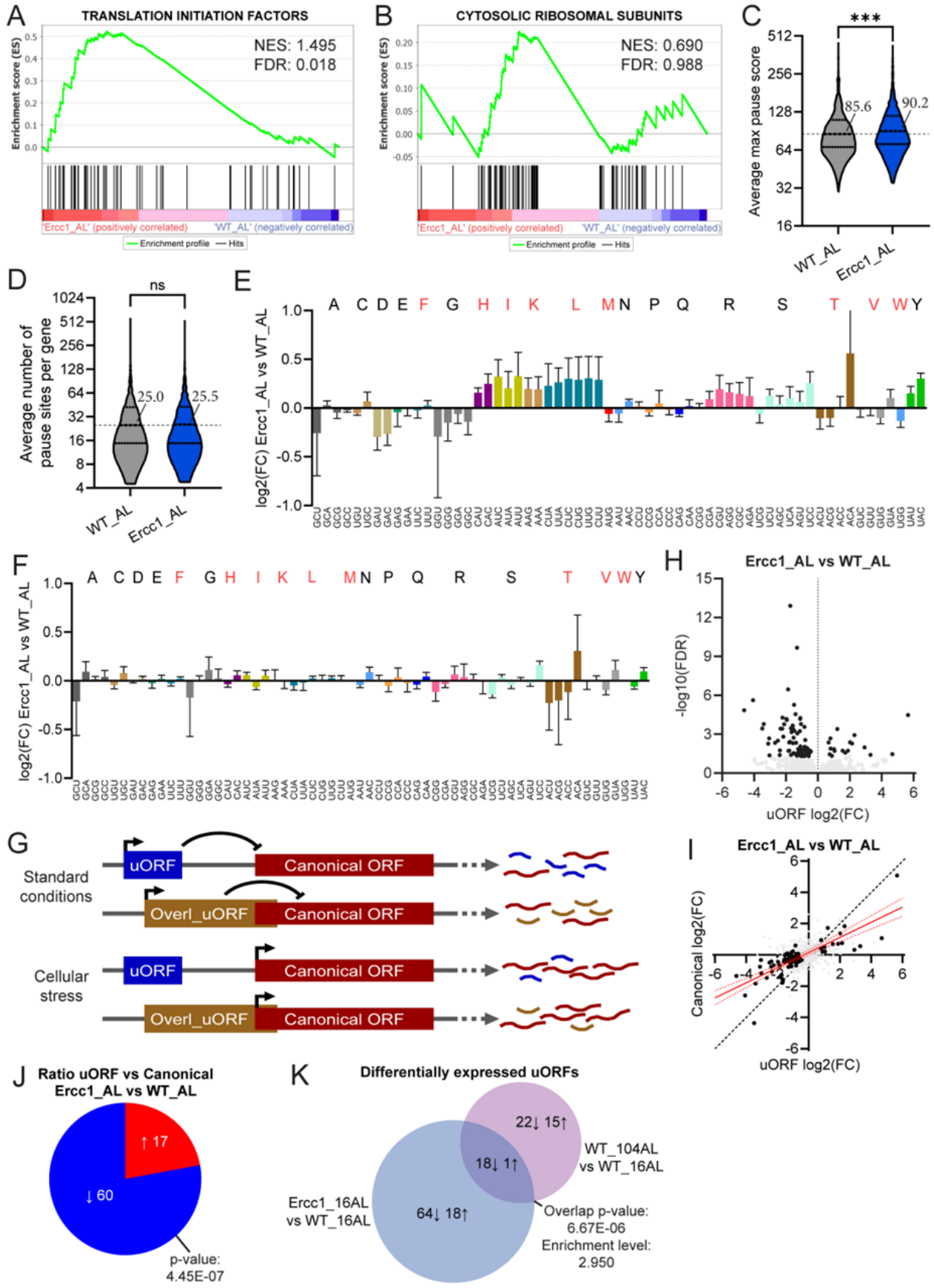
A
TRANSLATION INITIATION FACTORS
NES: 1.495
FDR: 0.018
Enrichment score (ES)
'Ercc1_AL' (positively correlated)
'WT_AL' (negatively correlated)
Enrichment profile
Hits
B
CYTOSOLIC RIBOSOMAL SUBUNITS
NES: 0.690
FDR: 0.988
C
***
Average max pause score
85.6
90.2
WT_AL
Ercc1_AL
D
ns
Average number of pause sites per gene
25.0
25.5
E
log2(FC) Ercc1_AL vs WT_AL
F
G
Standard conditions
Cellular stress
uORF
Canonical ORF
Overl_uORF
H
Ercc1_AL vs WT_AL
-log10(FDR)
uORF log2(FC)
I
Ercc1_AL vs WT_AL
Canonical log2(FC)
uORF log2(FC)
J
Ratio uORF vs Canonical
Ercc1_AL vs WT_AL
↑ 17
↓ 60
p-value:
4.45E-07
K
Differentially expressed uORFs
22↓ 15↑
WT_104AL
vs WT_16AL
18↓ 1↑
Ercc1_16AL
vs WT_16AL
64↓ 18↑
Overlap p-value:
6.67E-06
Enrichment level:
2.950

Figure 4

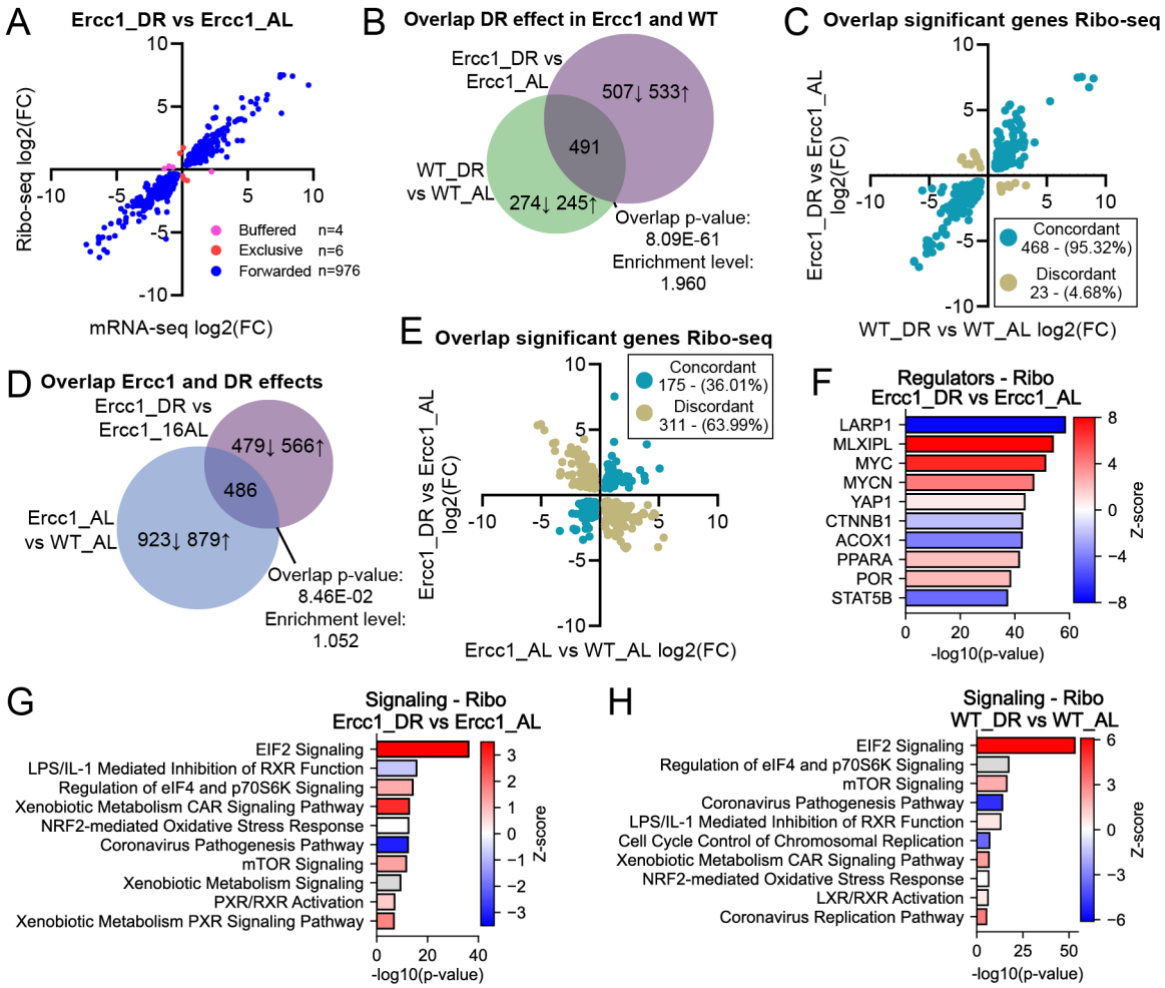
A
Ercc1_DR vs Ercc1_AL
Ribo-seq log2(FC)
mRNA-seq log2(FC)
Buffered n=4
Exclusive n=6
Forwarded n=976
B
Overlap DR effect in Ercc1 and WT
Ercc1_DR vs Ercc1_AL
507↓ 533↑
491
WT_DR vs WT_AL
274↓ 245↑
Overlap p-value: 8.09E-61
Enrichment level: 1.960
C
Overlap significant genes Ribo-seq
Ercc1_DR vs Ercc1_AL log2(FC)
WT_DR vs WT_AL log2(FC)
Concordant 468 - (95.32%)
Discordant 23 - (4.68%)
D
Overlap Ercc1 and DR effects
Ercc1_DR vs Ercc1_16AL
479↓ 566↑
486
Ercc1_AL vs WT_AL
923↓ 879↑
Overlap p-value: 8.46E-02
Enrichment level: 1.052
E
Overlap significant genes Ribo-seq
Concordant 175 - (36.01%)
Discordant 311 - (63.99%)
Ercc1_DR vs Ercc1_AL log2(FC)
Ercc1_AL vs WT_AL log2(FC)
F
Regulators - Ribo
Ercc1_DR vs Ercc1_AL
LARP1
MLXIPL
MYC
MYCN
YAP1
CTNNB1
ACOX1
PPARA
POR
STAT5B
Z-score
-log10(p-value)
G
Signaling - Ribo
Ercc1_DR vs Ercc1_AL
EIF2 Signaling
LPS/IL-1 Mediated Inhibition of RXR Function
Regulation of eIF4 and p70S6K Signaling
Xenobiotic Metabolism CAR Signaling Pathway
NRF2-mediated Oxidative Stress Response
Coronavirus Pathogenesis Pathway
mTOR Signaling
Xenobiotic Metabolism Signaling
PXR/RXR Activation
Xenobiotic Metabolism PXR Signaling Pathway
Z-score
-log10(p-value)
H
Signaling - Ribo
WT_DR vs WT_AL
EIF2 Signaling
Regulation of eIF4 and p70S6K Signaling
mTOR Signaling
Coronavirus Pathogenesis Pathway
LPS/IL-1 Mediated Inhibition of RXR Function
Cell Cycle Control of Chromosomal Replication
Xenobiotic Metabolism CAR Signaling Pathway
NRF2-mediated Oxidative Stress Response
LXR/RXR Activation
Coronavirus Replication Pathway
Z-score
-log10(p-value)

Figure 5

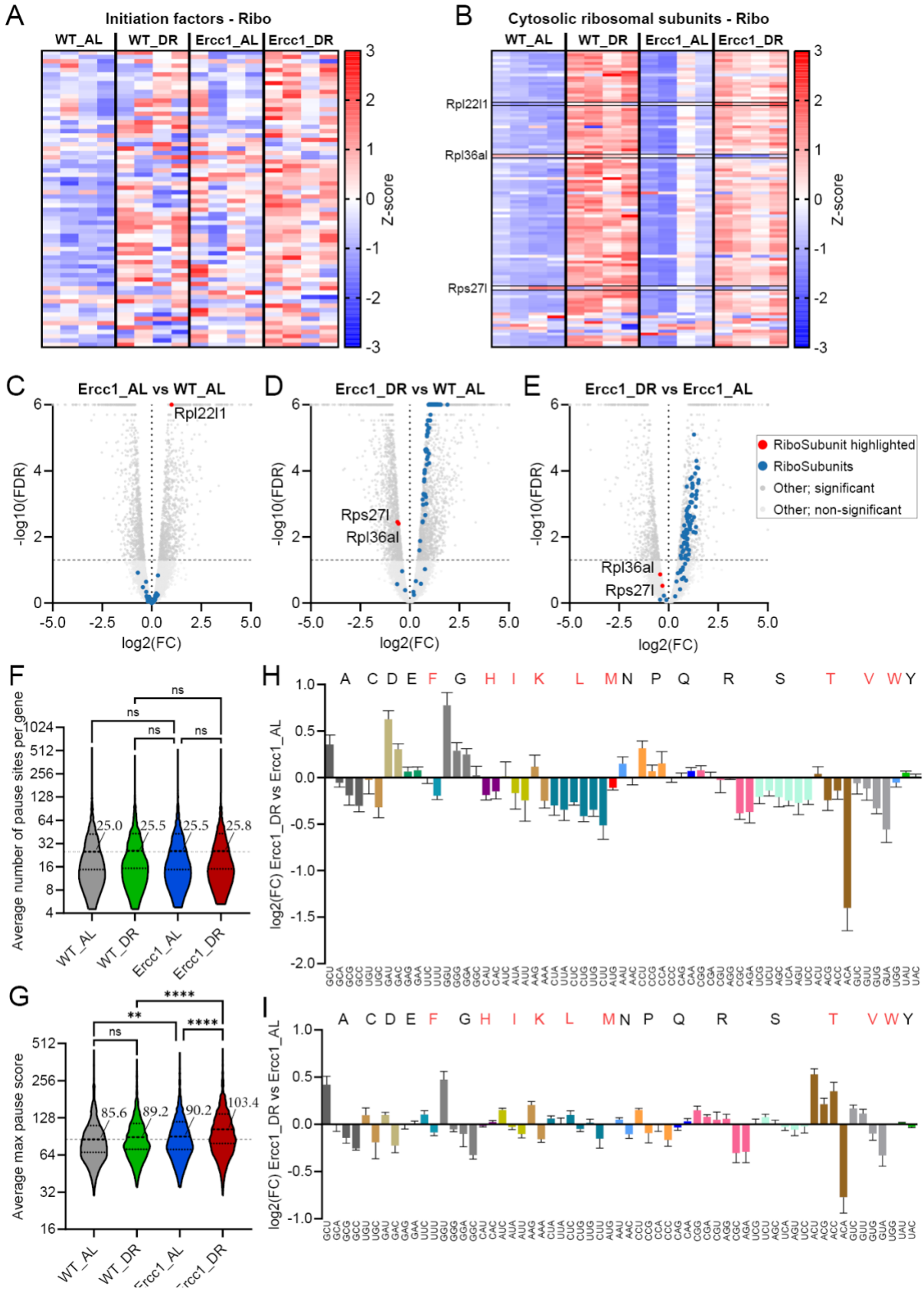
A
Initiation factors - Ribo
WT_AL
WT_DR
Ercc1_AL
Ercc1_DR
Z-score
B
Cytosolic ribosomal subunits - Ribo
Rpl22l1
Rpl36al
Rps27l
C
Ercc1_AL vs WT_AL
D
Ercc1_DR vs WT_AL
E
Ercc1_DR vs Ercc1_AL
-log10(FDR)
log2(FC)
RiboSubunit highlighted
RiboSubunits
Other; significant
Other; non-significant
F
Average number of pause sites per gene
ns
25.0
25.5
25.5
25.8
G
Average max pause score
****
**
85.6
89.2
90.2
103.4
H
log2(FC) Ercc1_DR vs Ercc1_AL
I

Figure 6

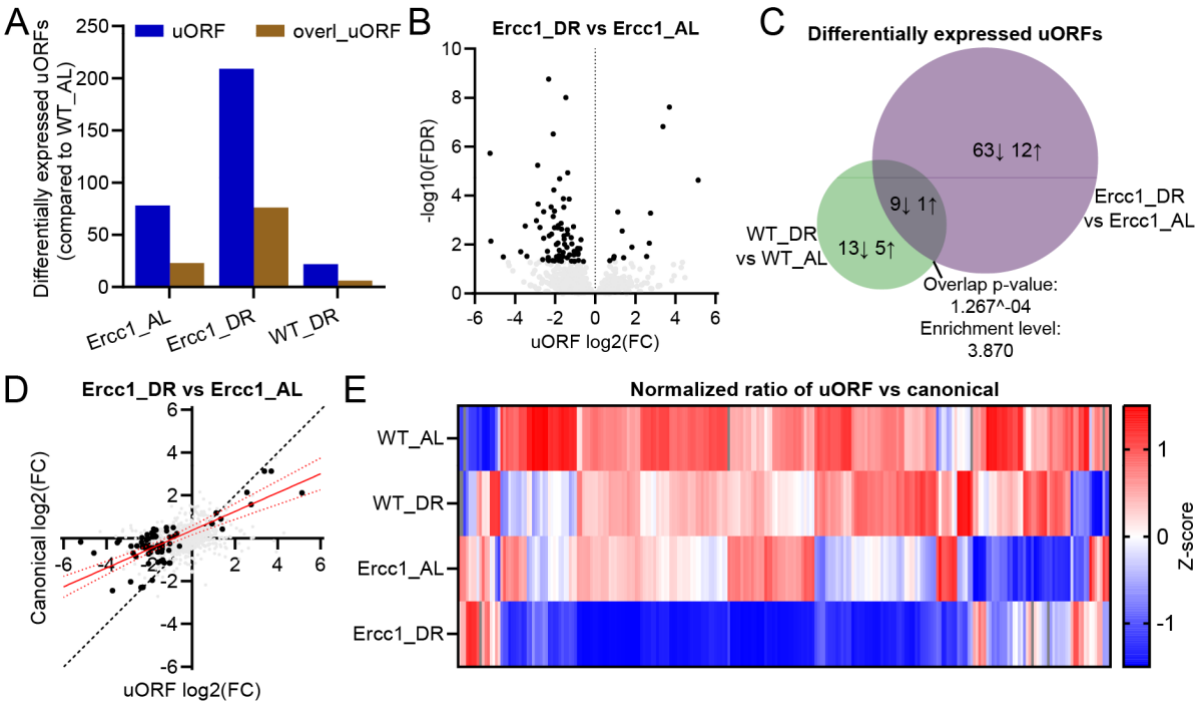
A
uORF
overl_uORF
Differentially expressed uORFs (compared to WT_AL)
250
200
150
100
50
0
Ercc1_AL
Ercc1_DR
WT_DR
B
Ercc1_DR vs Ercc1_AL
-log10(FDR)
10
8
6
4
2
0
-6 -4 -2 0 2 4 6
uORF log2(FC)
C
Differentially expressed uORFs
63↓ 12↑
9↓ 1↑
13↓ 5↑
Ercc1_DR vs Ercc1_AL
WT_DR vs WT_AL
Overlap p-value: 1.267^-04
Enrichment level: 3.870
D
Ercc1_DR vs Ercc1_AL
Canonical log2(FC)
6
4
2
-2
-4
-6
-6 -4 -2 2 4 6
uORF log2(FC)
E
Normalized ratio of uORF vs canonical
WT_AL
WT_DR
Ercc1_AL
Ercc1_DR
1
0
-1
Z-score